University of Illinois at Urbana-Champaign

ACRC

Air Conditioning and Refrigeration Center   A National Science Foundation/University Cooperative Research Center

Experimental Investigation of Viscous Two-Phase Flow in Microchannels

J. D. Burr, T. A. Newell, and P. S. Hrnjak

ACRC TR-252   June 2005

Abstract

Multi-port microchannel tubes are increasingly popular for use in a variety of heat transfer applications, primarily for automotive condensers and radiators, but also in a variety of refrigeration and air conditioning applications. These channels offer a greater surface area to volume ratio, providing for enhanced heat transfer over a conventional tube in many applications. Previous research has focused on characterizing the performance of such tubes for two-phase refrigerant flow. Most studies have focused on pure refrigerant flow, but in most applications, as a third viscous "phase" will be present in the form of lubricating oil. Much research has been done to account for the effects of increased viscosity due to the presence of oil in the flow, but the effects of viscosity in microchannels rather than larger conventional tubes remain largely unexplored.

The goal of this study is to investigate the qualitative and quantitative effects of the presence of oil within the refrigerant for two-phase flow in multi-port, extruded aluminum microchannel tubes. Three techniques are used to characterize these effects. Flow visualization experiments, using a transparent test section, demonstrate the flow configuration between the ports and flow regime within individual ports. Additionally, experimental adiabatic pressure drop and void fraction measurements – performed for a variety of fluids and flow conditions – quantitatively characterize the behavior of the refrigerant-oil mixture in two-phase flow.

Experimental results demonstrate a stark change in the flow when viscosity of the liquid phase is increased. These are noted by a change in the observed flow patterns, increased pressure drop, and depressed void fraction as compared to less viscous conditions. These trends cause significant departures from the behaviors characterized in many existing predictive correlations, and present a challenge to incorporate viscosity into modified correlations.

Table of Contents

List of Figures

List of Tables

Nomenclature

A	-Area (m^2)
D	-Diameter (m)
F_t	-Froude Rate
g	-Gravitational constant (9.81 m/s^2)
G	-Mass flux (kg/m^2s)
h	-Enthalpy (kJ/kg)
M	-Mass Fraction (-)
$\dot{m}$	-Mass flow rate (kg/s)
S	-Slip ratio (-)
x	-Quality (-)
X_{tt}	-Lockhart-Martinelli parameter
α	-Void fraction (-)
μ	-Dynamic viscosity ($N\text{-}s/m^2$)
ρ	-Density (kg/m^3)
cr	-Cross-sectional
h	-Hydraulic
l	-Liquid
v	-Vapor

Chapter 1. Introduction

1.1 Objectives

The primary goal of this study is to determine the effect of liquid-phase viscosity on two-phase flow in microchannels. Specifically, the channels in question are aluminum multi-port tubes, which are primarily used to construct heat exchangers for use in automotive applications, but because of the increased ratio of surface area to volume over conventional tubing, they are also attractive for other heating and cooling systems. The fluids of interest are refrigerants whose liquid phase viscosity is increased due to the presence of miscible or immiscible lubricating oil – usually present in relatively small quantities for most systems, but potentially having high concentrations at critical points such as the inlet of a condenser or the outlet of an evaporator.

Three experimental approaches are used in this study to capture the effects of liquid phase viscosity on two-phase flow in microchannels. Flow visualization provides for a determination of the flow regime present within each port of the microchannel, as well as the flow distribution between the several ports. Pressure drop measurements are made, as pressure drop is a key indicator of how much energy will be required to operate a system in which microchannels are utilized. Void fraction determinations likewise indicate the amount of refrigerant (and oil) in the microchannel at a given flow condition – thus leading to a prediction of refrigerant charge requirements for the system. The ultimate goal of such experimentation is to aid in the development of predictive correlations which will allow the system designer to better model the behavior of a system into which microchannels are incorporated.

1.2 Experimental Facility

To perform the experimentation described above, a "once-through" refrigerant flow facility, previously used for similar experimentation in pure refrigerant flow, was modified. The facility's lineage is detailed by Adams [1]. The system works without a compressor, unlike conventional systems both practical and experimental. Instead, the driving pressure for the flow is created between reservoirs at each end of the facility. This configuration allows for steady-state condition to be quickly reached for a wide range of flows, but also means that it is primarily useful for adiabatic two-phase flows at a selected constant quality.

The microchannels used for this study are extruded aluminum, and cut to lengths ranging from 7.62 cm to 106.68 cm. Two types of channel are used: a 6-port channel with a cross-sectional area, A_{cr}, of 16.7±0.1 mm^2 and a hydraulic diameter, D_h, of 1.54±0.02 mm; and a 14-port channel with cross-sectional area 15.0±0.1 mm^2 and hydraulic diameter 1.02±0.01 mm. These values were determined by examining high-resolution digital images of each cross-section, and calculating the area of each port as explained by Nino [5]. Images of the two cross-sections can be seen in Figure 1.1. Note that the nomenclature of microchannels is somewhat misleading, as it would seem to imply geometries on the order of 10^{-6} m; "micro" in this case instead simply means smaller than typical tubing. Figure 1.2 shows an illustration of how these microchannels are incorporated into a typical cross-flow heat exchanger.
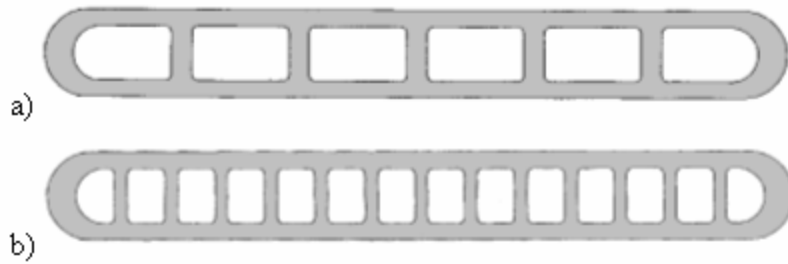
Figure 1.1: Cross-sectional images of microchannel geometry: a) 6-port, b) 14-ports.
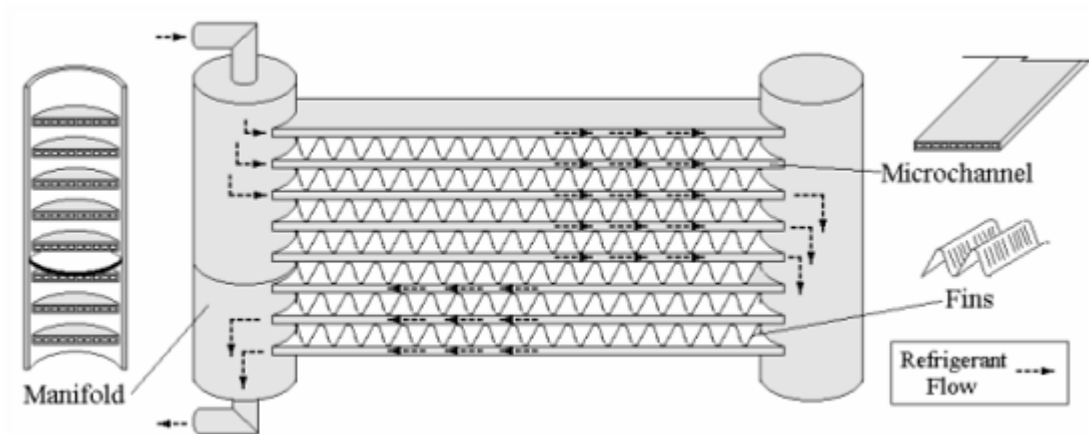
Figure 1.2: Heat exchanger constructed using microchannels.

1.2.1 Flow Visualization Test Section

In order to study the flow patterns of two-phase flows at various conditions, a transparent microchannel section constructed of PVC is utilized. The channel has 6 ports, and similar dimensions to the extruded aluminum 6-port channel: 1.58±0.06 mm hydraulic diameter and 17.0±1.2 mm^2 cross-sectional area. The channel is a two-piece design, with the ports machined out of the lower shell and a flat upper shell bolted on top of it containing the entrance and exit openings; a large O-ring maintains the pressure seal around the ports. Flexible hoses are used to connect the test section to the once-through loop. A Sony DCR TRV130 Hi-8 video camera is mounted directly above the test section, pointed down through the ports onto a white background. An Omega HHT31 variable frequency strobe light operated at 100 Hz provides illumination of this background, to isolate still images of the flow on film. Once the desired images are recorded, MGI Videowave 4 SE software is used to edit the video, and still images are culled from the digital archive using the image de-interlace function in Jasc Paint Shop Pro Version 7. An image of the flow visualization test section can be seen in Figure 1.3.
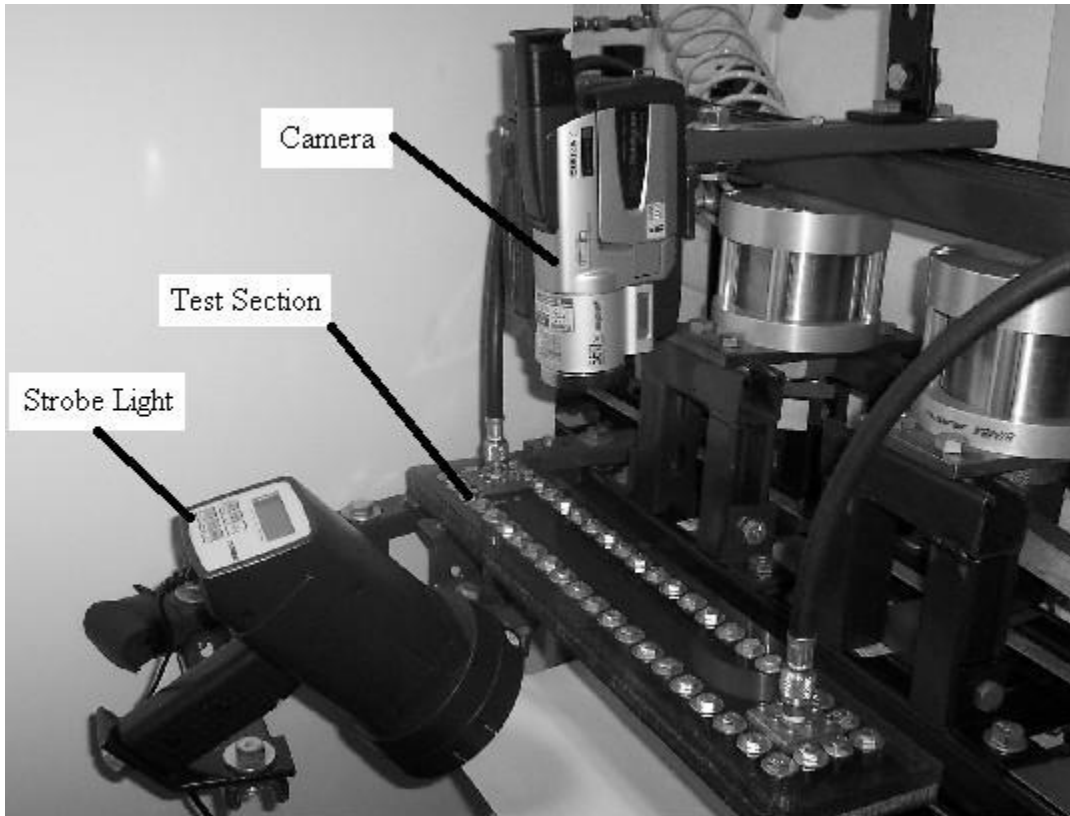
Figure 1.3: Image of the flow visualization experimental apparatus.

<u>1.2.2 Pressure Drop Test Section</u>

Figure 1.4 shows the test section used to collect pressure drop data for flow through the microchannel. A microchannel of any selected length is connected to the loop on each end using a transition section. This assembly is machined from aluminum to provide a smooth transition from the round tube of the loop to the flattened rectangular profile of the microchannel. The section is bolted together, and O-rings provide the seal as shown in the illustration of Figure 1.5. The transition section also provides for a tap, which allows the section to be connected to the pressure gauges. At the outlet of the pressure drop test section, a thermocouple provides a temperature reading. Thus, the pressure, pressure drop, and exit temperature for the flow are monitored and tabulated.
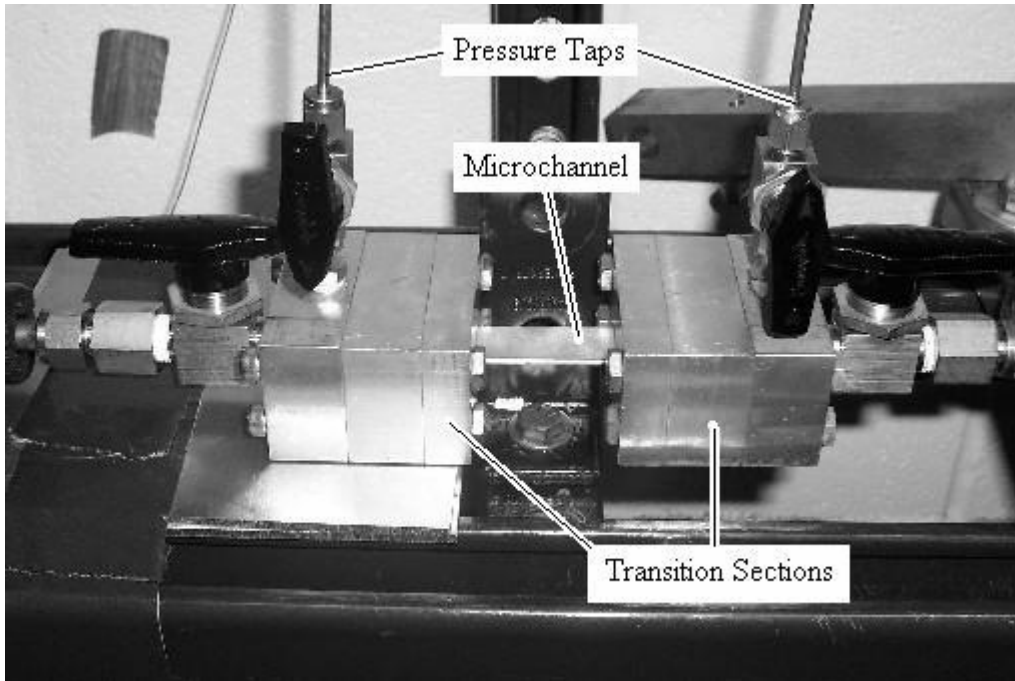
Figure 1.4: Pressure drop test section detail.
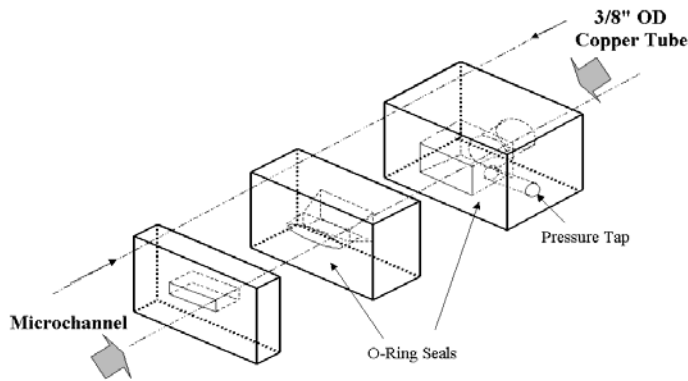
Figure 1.5: Illustration of the transition section assembly.

1.2.3 Void Fraction Test Section

The facility used for void fraction testing is depicted in Figure 1.6. Pneumatically actuated cylinders provide force via levers as shown, which direct rounded "blades" downward, simultaneously crushing both ends of the microchannel. The channel is held in place with the same transition sections described above. Once the channel is sealed, it can be removed from the section, so that its mass can be determined to facilitate void fraction calculation.
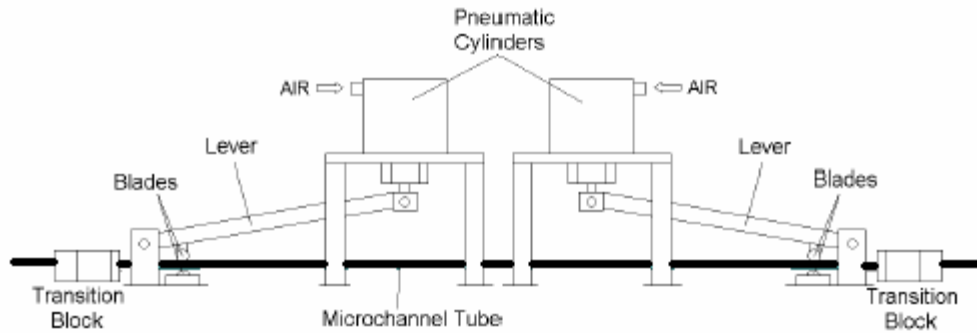
Figure 1.6: Schematic of the void fraction test section.

1.2.4 Flow Apparatus

As indicated above, the flow in the "once-through" loop is not circulated by a compressor; rather, a high-pressure reservoir is connected to the test section inlet, and a low-pressure reservoir at the test section outlet. Flow is thus naturally driven between the two reservoirs. The system provides two inlets: one each for vapor and liquid flow. A resistive heater is provided to ensure refrigerant in the vapor line maintains a slight super-heat and does not condense, while a simple counter-flow cold water jacket ensures sub-cooled liquid in the liquid line. In the case of air-oil experimentation, the vapor supply line is connected to a pressurized air system operating at approximately 800 kPa, while the same compressed air is used to pressurize a tank of oil. After the test section, the air-oil mix is vented to the atmosphere, with a reservoir to collect the oil and a filtering device to minimize oil mist outflow. For refrigerant flow, the source tanks are kept at or above room temperature (approximately 20°C) using a radiative heater, and the receiving tank is chilled in an ice-water bath to near 0°C. The resultant difference in saturation pressure drives the flow through the test section.

The relative amount of flow from each supply line is controlled using needle valves. The two streams are mixed, and proceed the through the test section, passing through a needle valve at the outlet, which controls the overall amount of flow, and in the case of refrigerant flow can be used to regulate the test section pressure by adjusting the pressure drop between the test section and the receiving tank. The sections of the loop between the reservoirs, exclusive of the test sections as described above, are constructed primarily of stainless steel (to allow the use of CO_2 in the facility), and the primary tube outside diameter is 9.53 mm (3/8").

1.2.5 Data Acquisition

To capture and record pertinent data on the flow, equipment is used as described below. For pressure drop data, and pressure measurements in the test section and in the vapor and liquid supply lines, Validyne DP-15 pressure gauges with replaceable diaphragms is used in conjunction with a Validyne CD280 four-input pressure transducer unit. The pressure gauges have accuracy of ±0.25% of the full scale range, with scales ranging from 14 kPa (for small pressure drop readings) to 3500 kPa (for absolute pressure readings). Temperature measurements at the same points in the facility are made using Omega CP+/CO- thermocouples, with accuracy of ±0.25°C. Mass flow readings are made using two Micro Motion Elite Sensors, Coriolis-type, with a model RFT9739 transmitter – one unit each for the vapor and liquid supply lines. These meters have accuracy of and ±0.50% for vapor ±0.10%

5

for liquid flow.   The signals for pressure, temperature, and mass flow are delivered to an Agilent 34970A Data Acquisition/Switch unit, connected to a standard PC running Labview Version 6i.

For the case of air-oil experimentation, the "quality" or mass fraction of the flow and the total mass flux are simple to calculate in Labview, using the two mass flow rates and the known area of the test section.

$$M = \frac{\dot{m}_v}{\dot{m}_v + \dot{m}_l} \qquad (1.1)$$

$$G = \frac{\dot{m}_v + \dot{m}_l}{A_{cr}} \qquad (1.2)$$

For refrigerant flow, the mass flux is calculated in the same fashion, but the quality is determined using an enthalpy balance on the flow as indicated in Equation 1.3. The enthalpy of the pertinent component is determined using pressure and temperature measurements in the supply line, with Labview calculating the enthalpy based on second-order curve fits in both temperature and pressure from the property data in the software program EES Version 7.

$$x = \frac{\dot{m}_v}{\dot{m}_v + \dot{m}_l} = \frac{h - h_l}{h_v - h_l} \qquad (1.3)$$

1.3 Experimental Procedures

1.3.1 Flow Visualization

To perform flow visualization trials, the equipment including camera, strobe, and test section, are configured as indicated in Figure 1.3. The flow facility is adjusted using the flow control valves to attain the desired conditions for mass flux and quality (or mass fraction), with the PC display updating the current conditions. With the room lights darkened and strobe light flashing at 100 Hz, the video camera is used to record approximately 20 seconds of video for archival and analysis. This is repeated at each desired flow condition. The test section can be arranged so that mesh screens are either present or absent at the channel inlet, to demonstrate the effect of inlet conditions on distribution of the flow between the ports.

Once the video is recorded, the processing software is utilized to save a digital copy of the footage, and also to capture screen shots representative of each flow condition. These still images contain two interlaced frames meaning that two images separated by 1/30 of one second exist in alternating columns of pixels. Thus the photo editing software is used to distill the image into one photograph for further analysis.

1.3.2 Pressure Drop

Pressure drop measurements are made by using the flow control apparatus to develop the desired quality and mass flux. Labview is used to record the output into a spreadsheet, with mass flows, temperatures and pressures recorded for each data point. Each trial consists of approximately 20 data points, with a sampling frequency of 1/3 Hz. To determine the pressure gradient along the length of the channel, or the differential pressure drop, data are taken twice over the same range of conditions: once with a 7.62 cm channel, and once with a 106.68 cm channel. To eliminate the effects of the transition sections, the pressure drop data from the former are subtracted from the

latter, and the resulting pressure drop, resulting from the 99.06 cm difference, can be divided by this length to give differential pressure drop in units of kPa/m.

1.3.3 Void Fraction

The trapping or "crimping" apparatus described above is used to determine the void fraction for refrigerant flows. In the case of air-oil experimentation, the void fraction is completely equivalent to oil holdup, and for refrigerant-oil experiments, oil holdup, or the fraction of oil in the channel at steady state, is also of crucial interest. The 106.68 cm channel of either 6- or 14-port configuration is fixed in the loop as previously described, and the desired flow conditions are developed in the once-through loop, monitored via Labview. Once a steady flow is reached, a standard 110 VAC circuit is used to activate solenoid valves for each pneumatic cylinder, and the resulting motion of the lever arms causes the channel to be sealed at each end. The current is then shut off, causing the levers to retract, and the channel can be removed from the loop. The channel's mass is recorded prior to being placed in the loop, and then after it is sealed. The difference represents the total mass trapped between the sealed points. For air-oil experiments, this is sufficient to determine the void fraction or oil holdup, since the air mass is negligible compared to that of the oil. For refrigerant-oil testing, the channel is punctured to allow any trapped refrigerant to escape. The mass is then determined for a third time, for just the oil held up.

Chapter 2 Flow Visualization

2.1 Background

In order for reliable predictive correlations for quantities such as pressure drop and void fraction to be formed for two-phase flow, it is beneficial to include in the development of these correlations a dependence on flow regime. Flow visualization is the most practical method of making observations on the flow regime dominant at a given set of conditions. However, as described by Nino [5], few previous studies have taken into account the effects of having flow in multiple parallel ports, as is the case with microchannels.

The main outcome of the work in this area by Nino was the development of a system of statistical flow regime prediction, in the form of functions describing the time fraction in which a given flow regime would be expected to appear for a specified quality and mass flux. However, this is a time-consuming process, and one which is susceptible to human error due to the somewhat subjective nature of the classification of flow regimes. One possibility under development is automated flow regime detection, which would use optical instruments linked to software capable of both detecting flow patterns and gathering a statistically significant set of data for predictive purposes.

For this study, a qualitative analysis outlines the general trends which can be expected due to the influence of increased liquid-phase viscosity due to the presence of lubricants. The transparent PVC microchannels described previously are used, along with inlet screens to vary the flow pattern entering the channel. While the PVC test section was created to closely mimic the geometry of the aluminum microchannels that are the focus of this research, it is impossible to replicate the exact inlet conditions of the transition sections; therefore the presence or absence of screens creates a reasonable estimate of how well- or poorly-mixed the flow in the actual microchannels may be.

It is important to define the nomenclature to describe the flow regimes under consideration. Coleman and Garimella [3] divided flow in small channels into four types, as illustrated in Figure 2.1. These descriptions will be utilized in the following discussion. The stratified regime is characteristic of flows with low Reynolds number; it is not observed in microchannels due to the small diameters of the ports. The intermittent regime is characterized by liquid and vapor moving together with the same velocity. Annular or wavy annular flow typically arises at higher mass fluxes, as the liquid and vapor phases separate and move at different velocities. The dispersed flow regime is similar in nature to the intermittent regime, but is not typically observed in the microchannels under consideration. Thus, intermittent or homogeneous and annular or separated flows are the principle patterns of interest in this investigation.
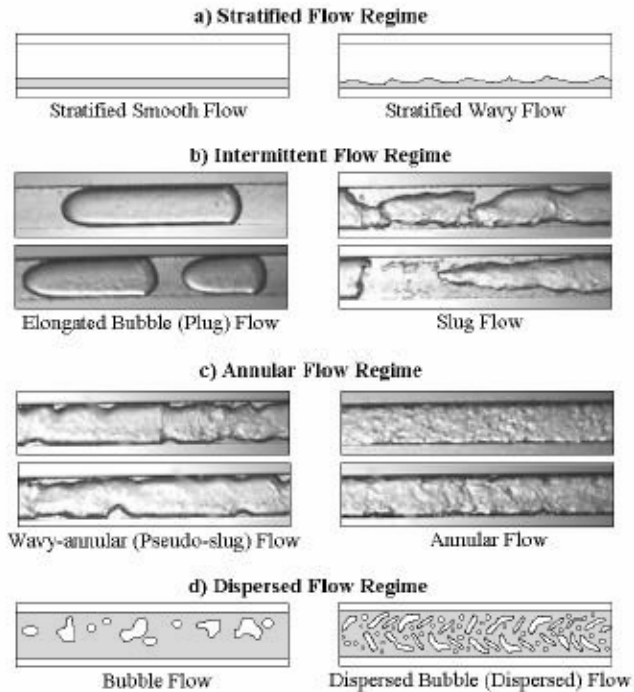
Figure 2.1: Flow regime classification chart.

2.2 R22 Results

In order to build on the archive of flow visualization for the microchannels of this study, which was begun by Nino, experimentation was performed with pure R22 prior to the addition of oil. These results also provide a basis for comparison of the air-oil and refrigerant-oil flow visualization described below. R22 flow is depicted in two configurations: Figure 2.2 shows flow without inlet screens, and Figure 2.3 depicts flow with inlet screens. (Figures follow the body of this chapter, due to their large size.) Two general trends are worth noting, as they are indicative of changes in other aspects of the flow. As quality increases, the homogeneous flow pattern disappears, and is replaced entirely with annular flow. This is indicative of a higher overall slip ratio, or difference between vapor and liquid velocities, which implies a greater liquid-phase holdup will occur. Also, the surface of the two-phase interface appears more "rippled" at higher mass fluxes, implying a more turbulent vapor core interacting with the liquid. Increased pressure drop is attributable to this phenomenon, as will be demonstrated in the pressure drop results. It is impossible, however, to draw more concrete inferences from the static images displayed below. The nature of two-phase flow in microchannels gives rise to mal-distributions across the several ports, causing different flow regimes to simultaneously appear in the channel. For this reason, the automation of a statistical flow regime detection system is highly desirable to better characterize the flow.

2.3 Air-Oil Results

To isolate the effects of liquid-phase viscosity on the visible flow field, experimentation was performed with air and alkylbenzene of several viscosity grades. Figure 2.4 shows the flow for air and ISO-32 alkylbenzene across several mass fractions at three different mass fluxes. The results are similar to those seen with pure R22, but with more stark realization of the same trends described for that case. Figure 2.5 shows this flow with similar

9

conditions, but different inlet configurations. The effect on distribution between the ports is clear: the presence of the entrance screens serves to better mix the incoming flow and distribute it among the ports. The screens virtually eliminate the homogeneous flow pattern in this case, in contrast to the unscreened flow. Figure 2.6 depicts the influence of viscosity, which is surprisingly limited. In light of the heavy influence of viscosity on the qualitative results of later sections, the implication is that while flow pattern may have a large influence on quantities such as pressure drop and void fraction, it is not always a reliable predictor of changes due to factors such as viscosity.

2.4 Refrigerant-Oil Results

Figure 2.7 gives flow visualization results for a combination of vapor R22, and a liquid phase of R22 with 36.3% by mass ISO-32 alkylbenzene. ASHRAE Standard 41.4-1984 [2] is followed for this and all subsequent oil concentration determinations. Similar trends to those described above are observed. Note that the observations are limited to the high-quality region, where an oil-rich liquid phase is likely to be observed, for instance near an evaporator outlet or condenser inlet in a real system. As with the pure refrigerant, as compared to the air-oil mixture, there is a greater effect from mass flux in this case than on inlet conditions. This implies that the inlet conditions will only be of great importance for the overall flow field in the highly viscous case of the air-oil experimentation. Figure 2.8 shows the results of a similar trial using R134A with a 86.7% by mass ISO-32 POE liquid phase.
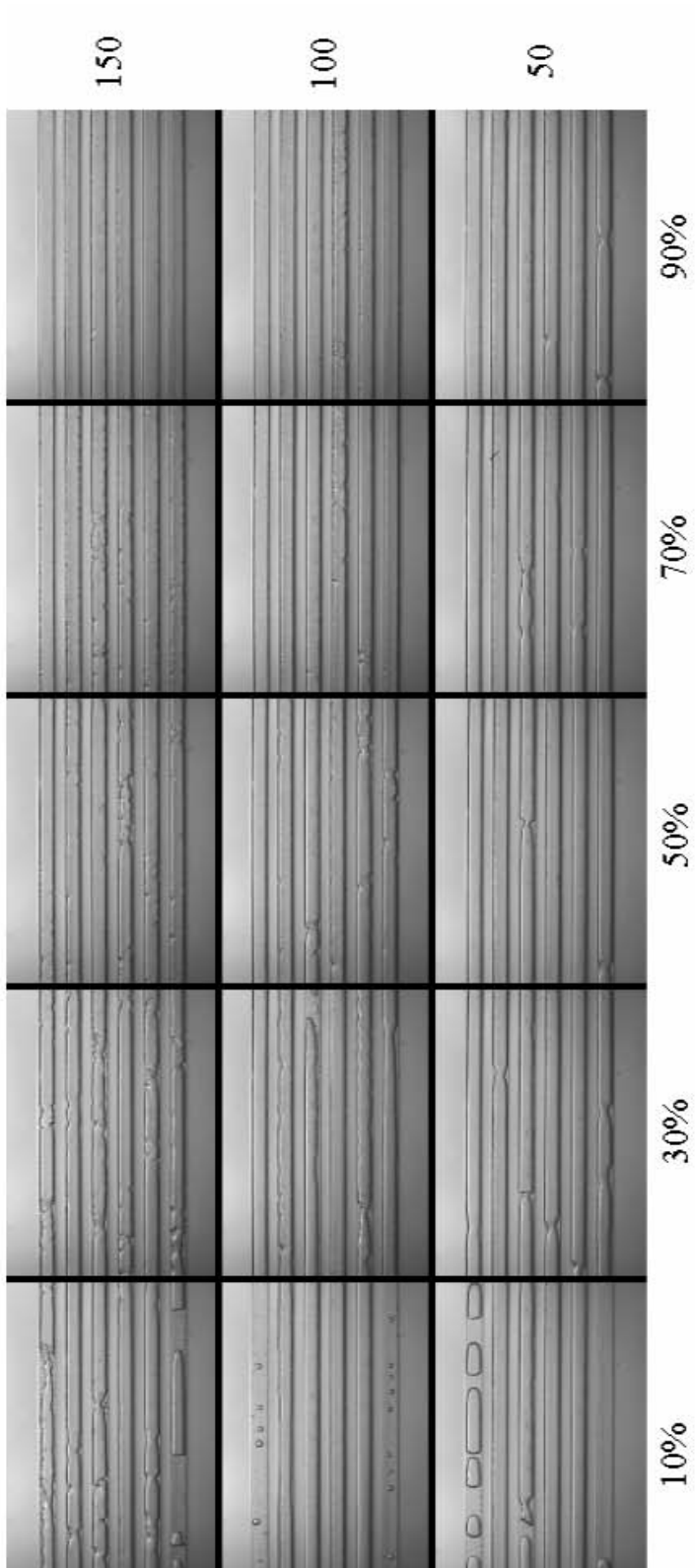
Figure 2.2: R22 (quality, mass flux) without inlet screens.
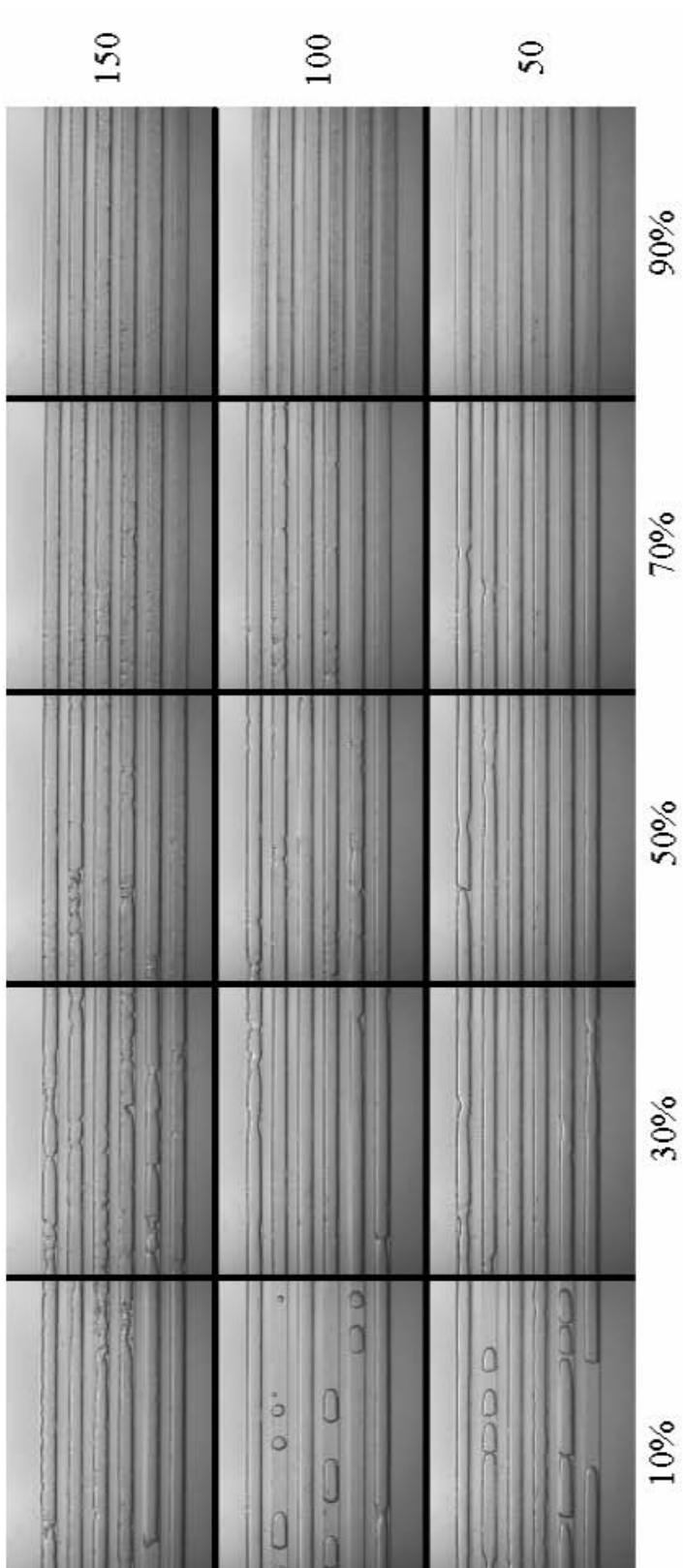
Figure 2.3: R22 (quality, mass flux) with inlet screens.
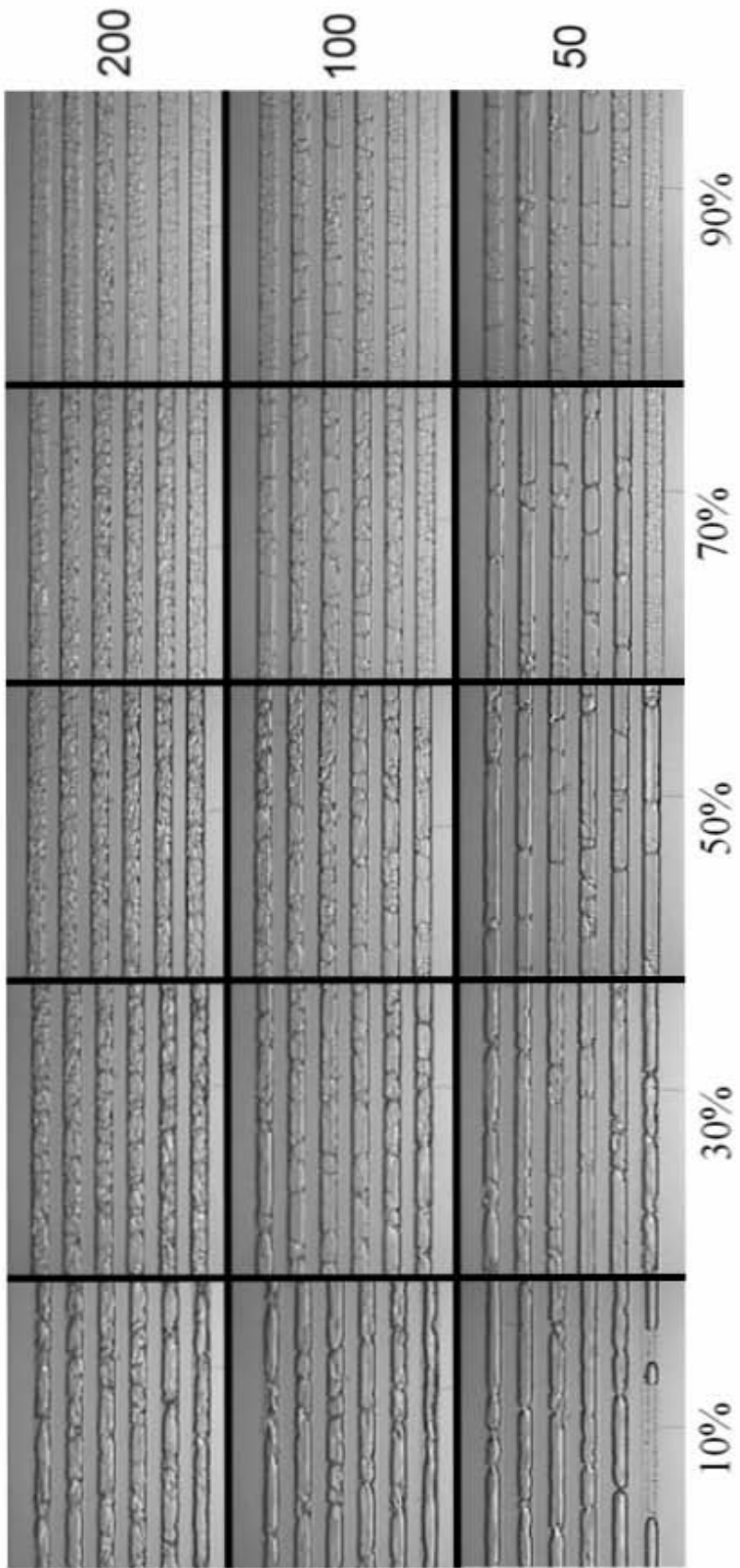
Figure 2.4: Air-ISO-32 alkylbenzene (mass fraction, mass flux), with inlet screens.

13
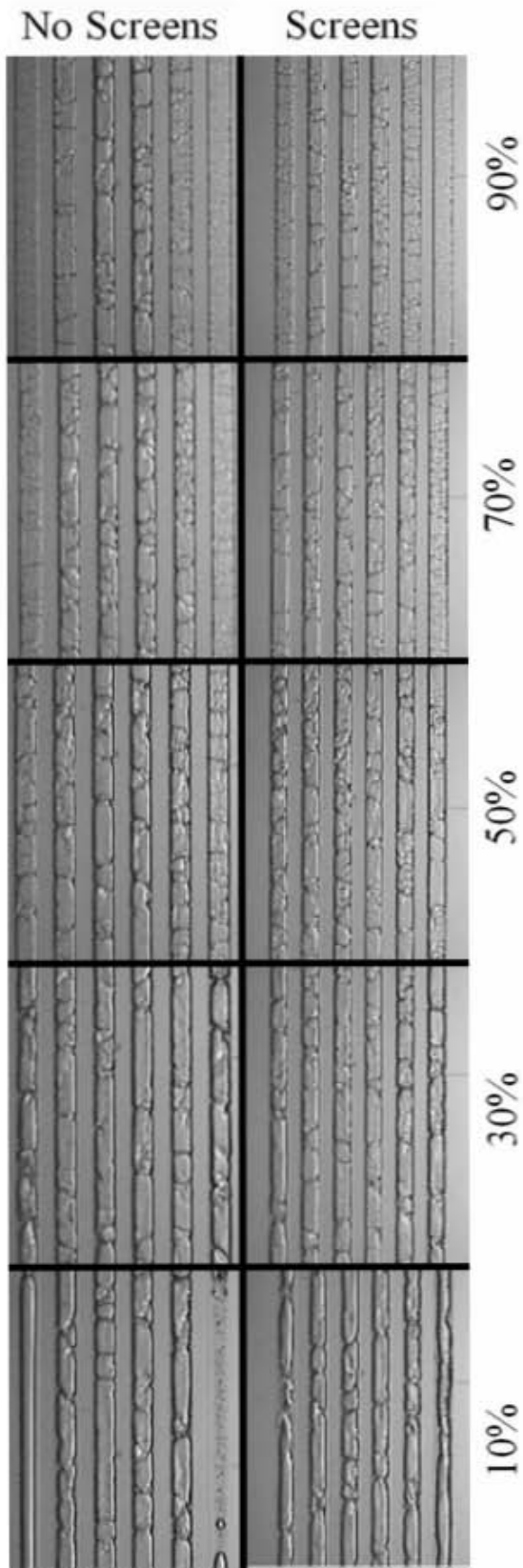
Figure 2.5: Air-ISO-32 alkylbenzene (mass fraction, G=50), with & without screens.
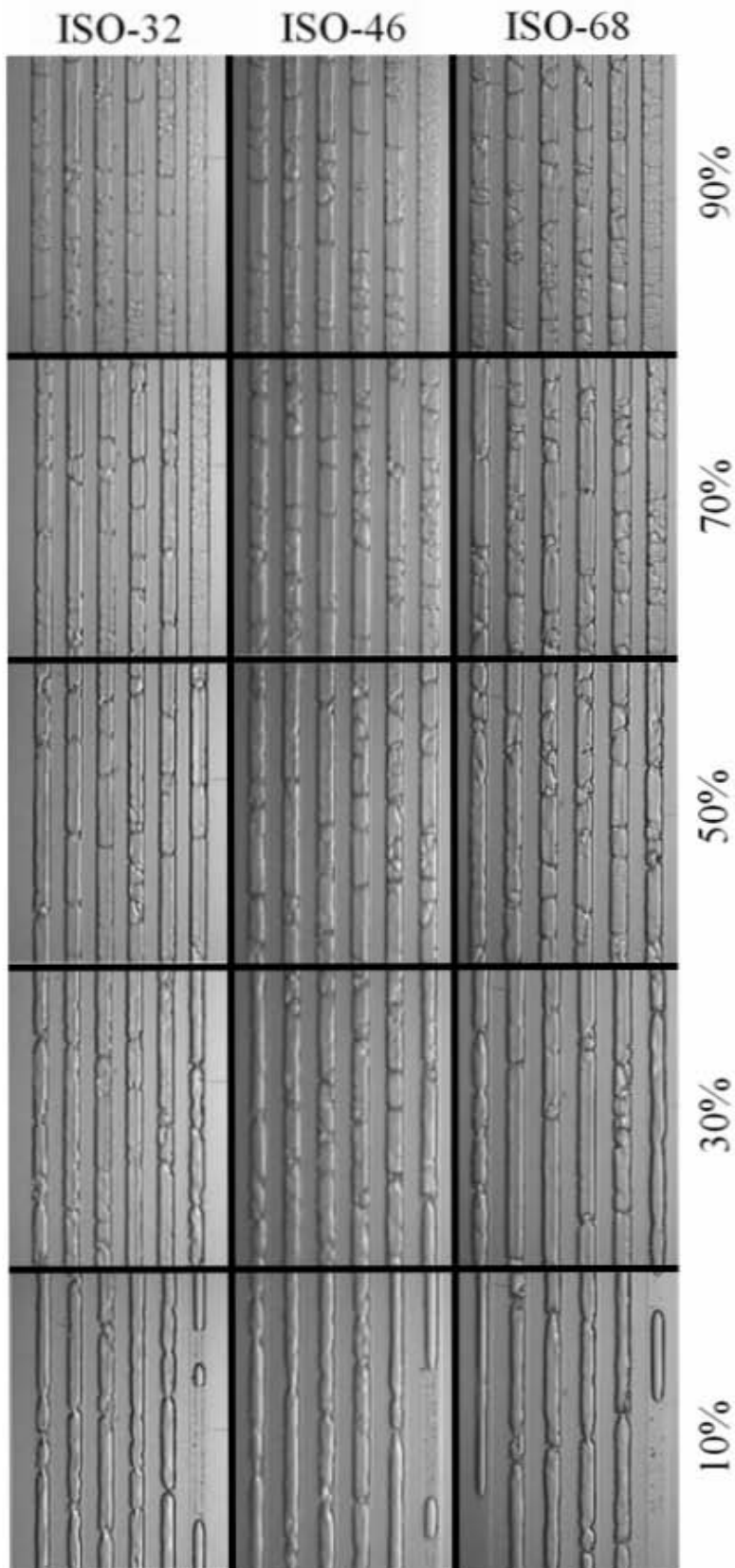
Figure 2.6: Air-oil (mass fraction, viscosity), G=50.
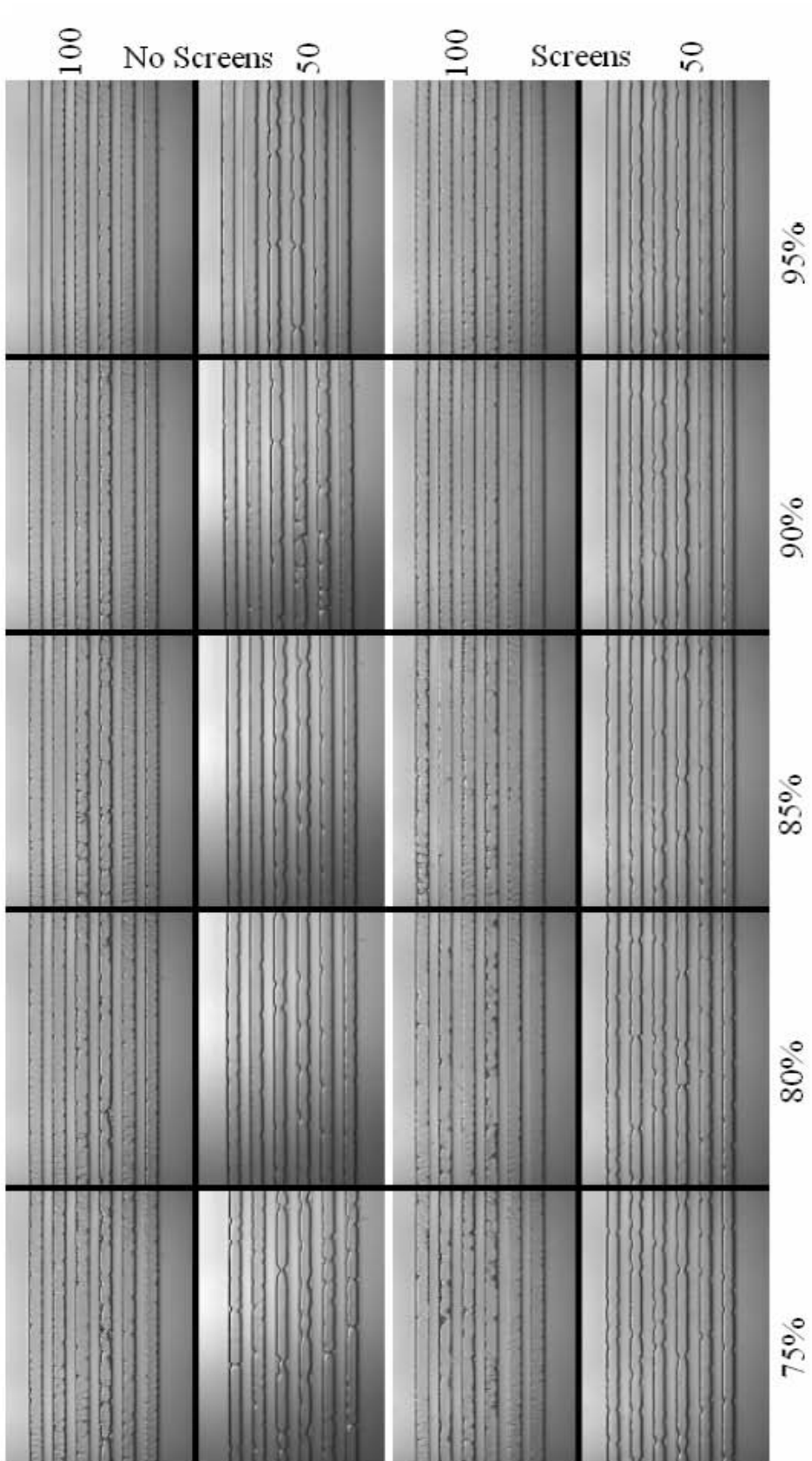
Figure 2.7: R22-ISO 32 alkylbenzene (quality, mass flux, inlet configuration).
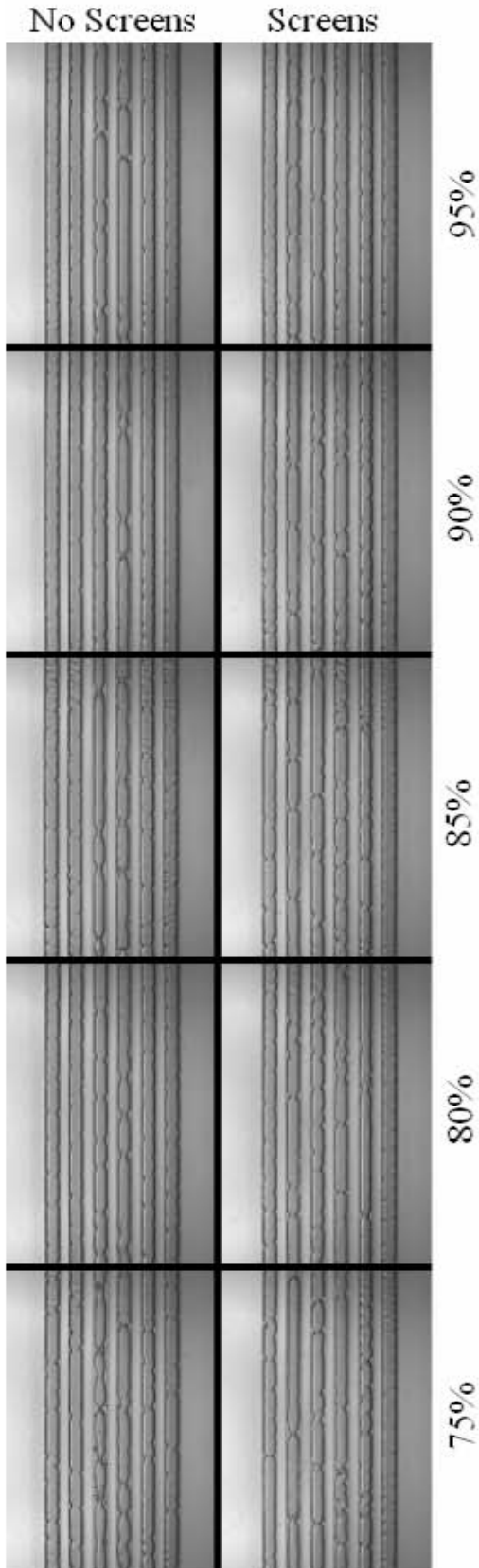
Figure 2.8: R134A-POE (quality, inlet configuration), G=50.

Chapter 3 Pressure Drop

3.1 Background

Pressure drop is of primary interest in the characterization of two-phase flow in microchannels, particularly in the design of heat transfer systems which utilize these channels, since pressure drop is directly indicative of the amount of energy required to circulate the working fluid through the system. As indicated by Nino [5], most predictive correlations for two-phase flow do not incorporate the effects unique to flow in small-diameter channels, and those that do focus on such channels are typically only applicable over the limited range of geometries for which they were developed. Thus the work of both Nino and Adams [1] focused on developing a predictive pressure drop correlation for multi-port microchannels. Adams describes relations suitable for both the homogeneous and separated regimes. However, none of these relations provides for the incorporation of parameters such as viscosity and surface tension, associated with the presence of a lubricant in the liquid phase.

3.2 R22 Results

Just as in the flow visualization experimentation, pressure drop determination was performed with pure R22, both as general reference and as a baseline for comparison of results incorporating oil. Figure 3.1 gives differential pressure drop for R22 at three different mass fluxes over the complete range of quality. As described in the procedure, it is necessary to subtract two discrete sets of data to determine the differential pressure drop. The curves depicted in Figure 3.1 represent the difference between the least-squared-error curve fits of these two sets of data for each mass flux. This procedure is repeated for clarity for all remaining pressure drop graphs. It is important to note that these represent curve fits to experimental data, not charts of predictive correlations. Points represent adjusted data, with error bars representing ± two standard deviations from the mean recorded value. These give an indication of the short time scale fluctuations in pressure drop, which are likely the result of plugging of individual ports and other such non-uniformities in the flow. This explains the larger fluctuations at lower qualities, where homogeneous flow is more prevalent. These fluctuations are nearly always greater than the experimental uncertainty of the measured pressure drop. Appendix A gives the complete uncorrected data sets for both long (106.68 cm) and short (7.62 cm) test sections for all pressure drop experimentation.
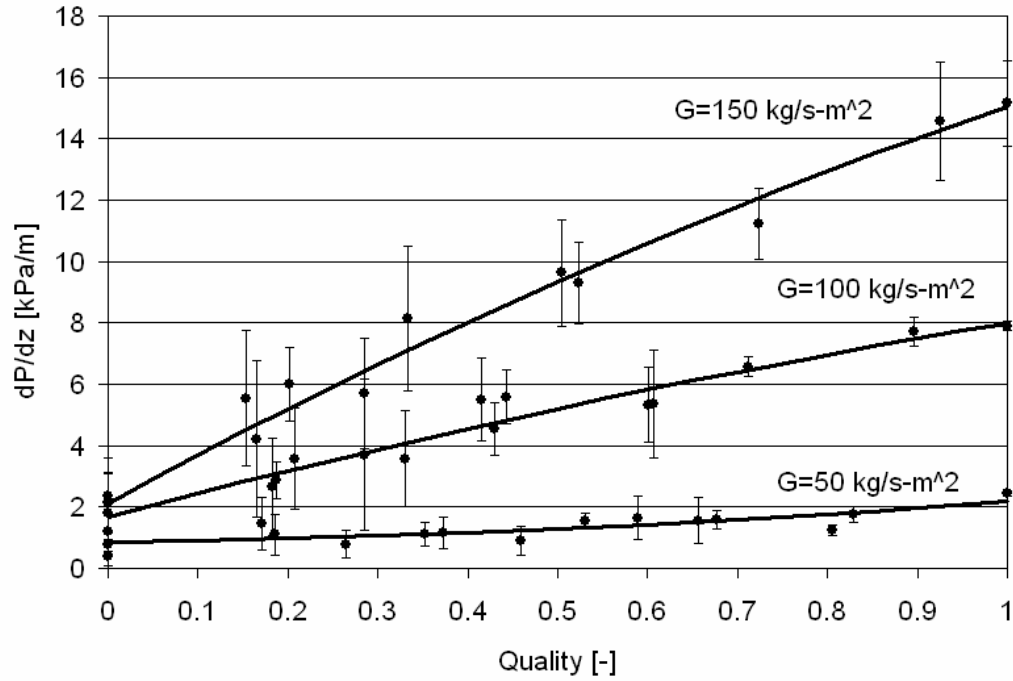
Figure 3.1: R22 differential pressure drop, 14-port.

3.3 Air-Oil Results

Figures 3.2 through 3.5 give the results of pressure drop experimentation for air-alkylbenzene combinations of varying viscosity index. These graphs demonstrate the difficulties associated with matching existing predictive correlations for two-phase flow in microchannels with flows having increased liquid-phase viscosity. The primary difficulty stems from the greatly increased magnitude of the liquid phase, as illustrated for low mass fraction points. Also, the greatly exaggerated peak at the high-quality range is indicative of the loss of potential created by interactions between the vapor and liquid at the interface, as alluded to in the flow visualization section.
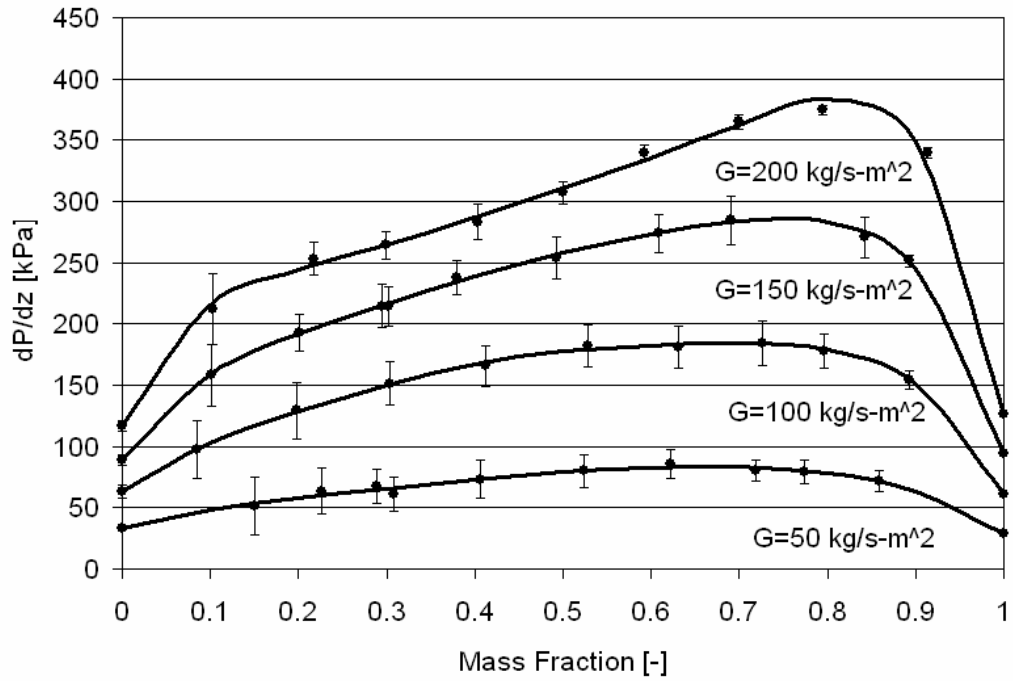
Figure 3.2: Air-ISO-10 alkylbenzene pressure drop, 14-port.
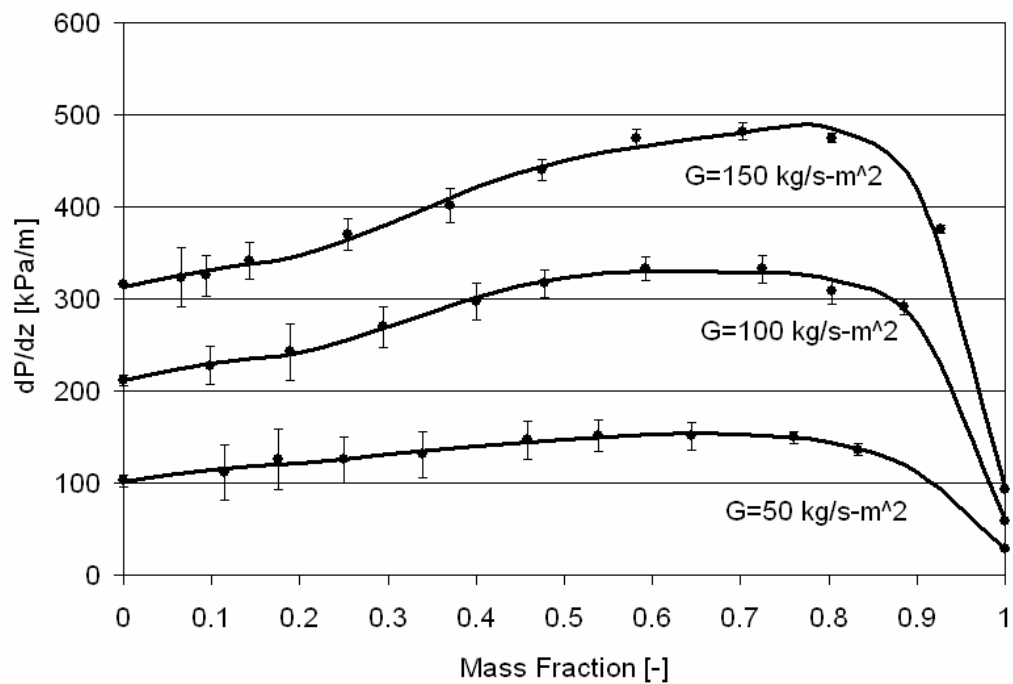
Figure 3.3: Air-ISO-32 alkylbenzene pressure drop, 14-port.
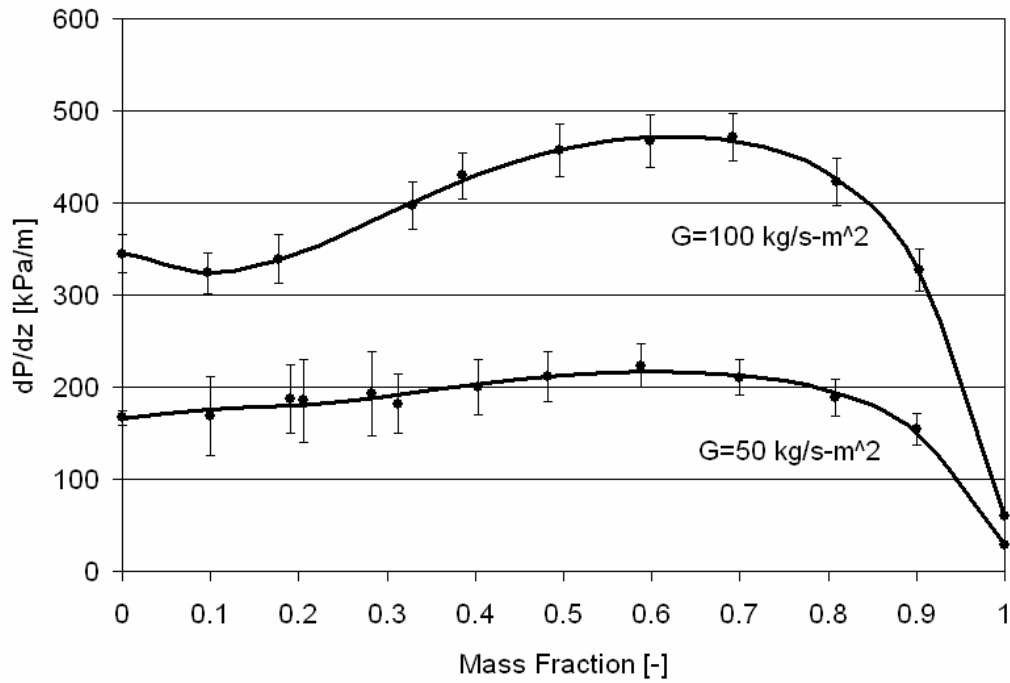
Figure 3.4: Air-ISO-46 alkylbenzene pressure drop, 14-port.
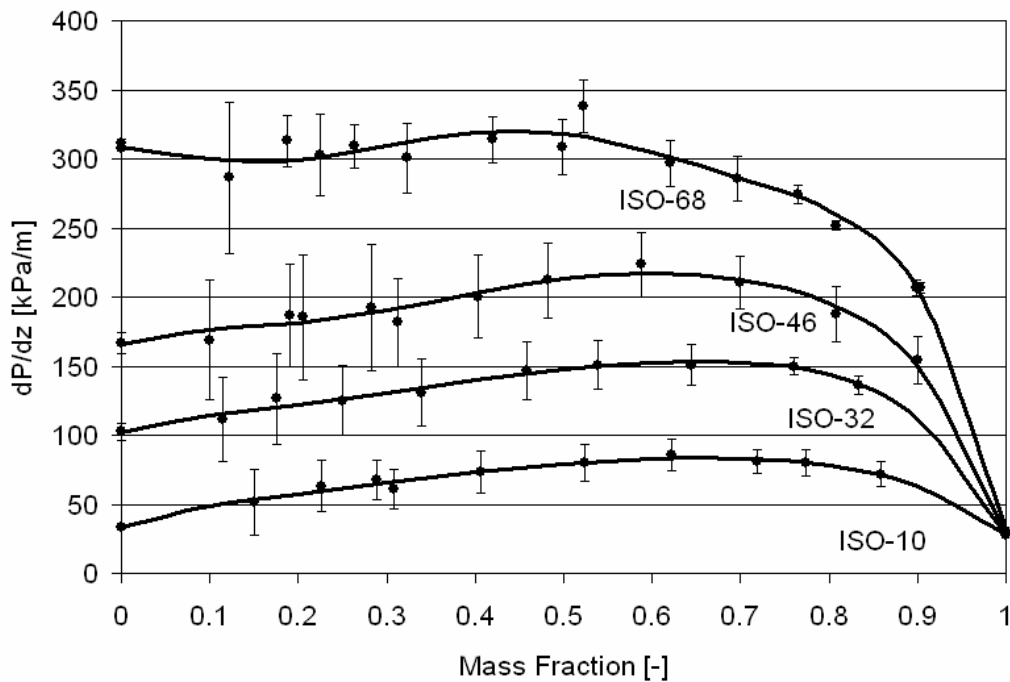
Figure 3.5: Air-alkylbenzene pressure drop, G=50, 14-port.

3.4 Refrigerant-Oil Results

The viscosities of the liquid phases examined above are admittedly dissimilar to the conditions found in a typical system, particularly when considering the difference in thermo-physical properties between the oil and the

air. A more realistic case is demonstrated in Figure 3.6, with a 36.3% ISO-32 alkylbenzene liquid R22 phase compared to the pure case. The departure from the pure behavior exemplifies the increased pressure drop caused by the presence of lubricant. Figure 3.7 gives a sense of the influence of the lubricant's concentration and viscosity, by comparing the pure and ISO-32 cases with an ISO-10 alkylbenzene at 52.2% by mass in the liquid phase. As expected, the lower-viscosity oil causes a pressure drop between the other cases. Lastly, the effect of oil miscibility is demonstrated in Figure 3.8, using R134A with both a miscible (86.7% ISO-32 POE) and immiscible (100% ISO-32 alkylbenzene) lubricant. Again, as expected, the immiscible alkylbenzene creates a greater pressure drop. Note that the concentrations listed represent the mass percentage of oil in the liquid phase entering the test section, not the overall concentration in the flow.
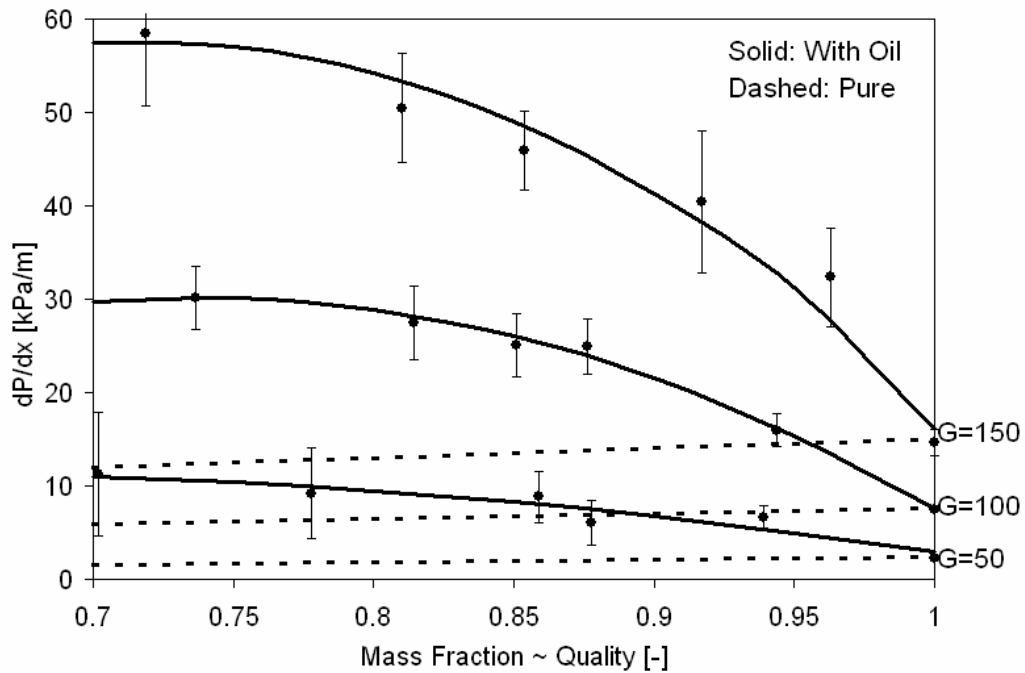
Figure 3.6: R22 pressure drop, with 36.3% liquid ISO-32 alkylbenzene, 14-port.
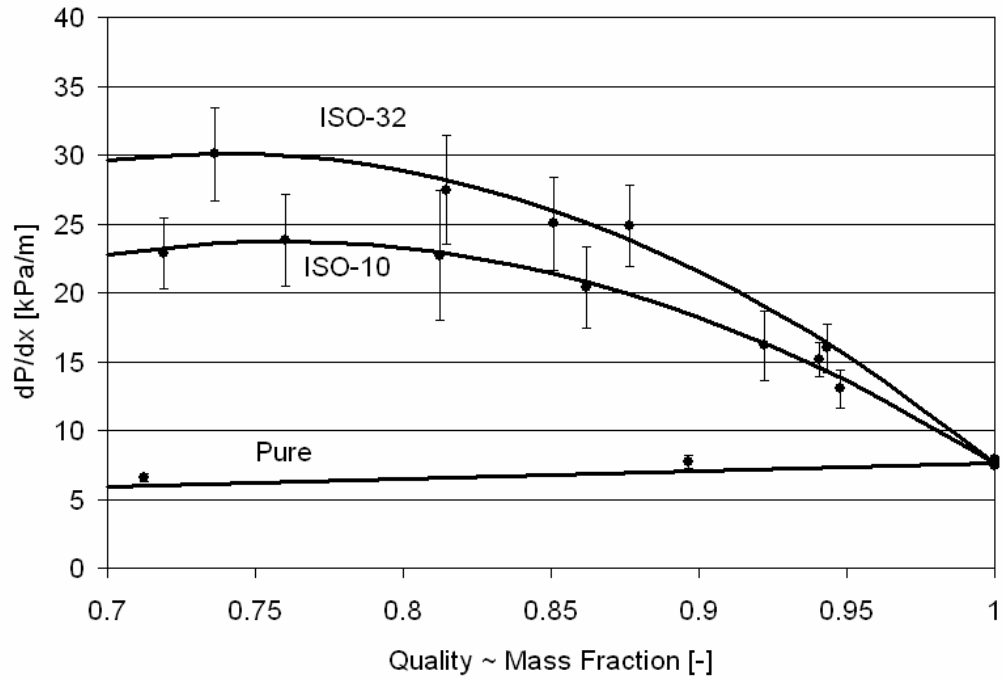
Figure 3.7: R22 pressure drop with varying oil content, 14-port.
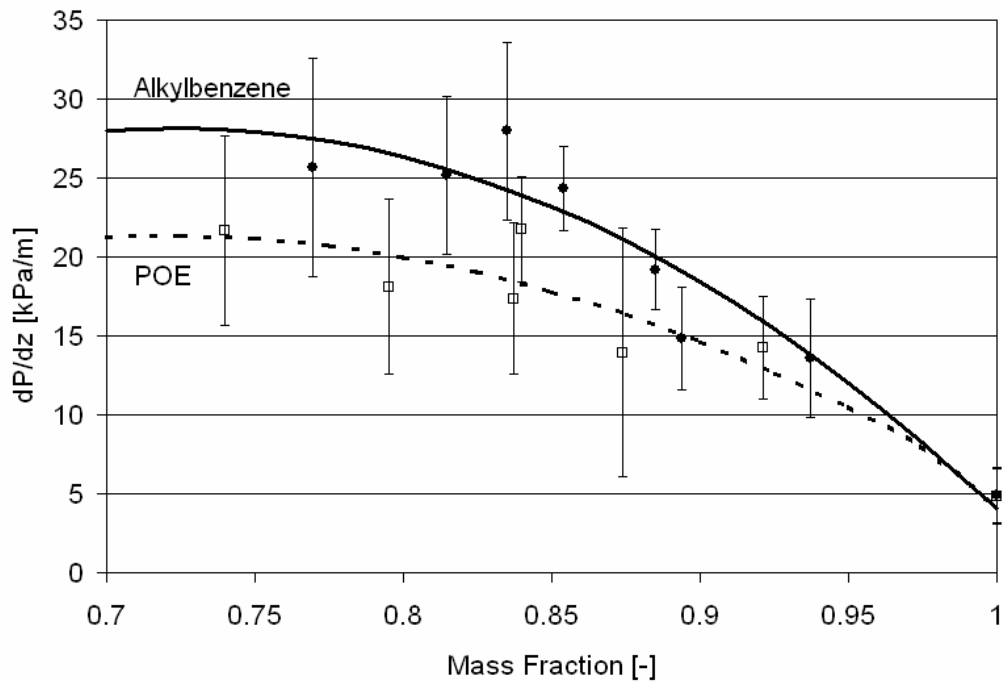
Figure 3.8: R134A pressure drop with ISO-32 alkylbenzene and ISO-32 POE, 14-port.

Chapter 4 Void Fraction

4.1 Background

Void fraction is a key parameter in the determination of charge requirements for a system. As microchannels become increasingly prevalent in practical systems, it is therefore desirable to predict the amount of refrigerant charge needed, as well as the impact of dissolved lubricant on the distribution within the system.

Several models of void fraction for two phase flow have been developed. One of the simplest is described as the homogeneous relation [Nino, 5]; as the name implies it does not account for a variation of velocity between the two phases. Equation 4.1 gives this relation.

$$\alpha = \frac{1}{1 + \frac{1-x}{x}\frac{\rho_v}{\rho_l}} \tag{4.1}$$

Crompton [4] describes two improved correlations. The first, from Zivi, takes into account the relative velocities of the two phases in the form of S, the slip ratio of vapor to liquid velocity. Equation 4.2 gives the relation, and Equation 4.3 the form used to predict S in the Zivi correlation.

$$\alpha = \frac{1}{1 + \frac{1-x}{x}\frac{\rho_v}{\rho_l}S} \tag{4.2}$$

$$S = \left(\frac{\rho_l}{\rho_v}\right)^{1/3} \tag{4.3}$$

The second, the ACRC correlation, takes into account the mass flux and uses Xtt, the Lockhart-Martinelli parameter, as indicated in Equations 4.4-4.6.

$$\alpha = \left(1 + X_{tt} + \frac{1}{Ft}\right)^{-.321} \tag{4.4}$$

$$X_{tt} = \left(\frac{1-x}{x}\right)^{.9}\left(\frac{\rho_v}{\rho_l}\right)^{.5}\left(\frac{\mu_l}{\mu_v}\right)^{.1} \tag{4.5}$$

$$Ft = \left(\frac{x^3 G^2}{\rho_v g D(1-x)}\right)^{.5} \tag{4.6}$$

Note that of these correlations, only the ACRC correlation takes viscosity into account.

4.2 Air-Oil Results

Figures 4.1 and 4.2 show results for void fraction testing using air and ISO-32 alkylbenzene as the vapor and liquid. While typical two-phase refrigerant flows demonstrate void fractions well above 80-90% over a broad range of qualities, the primary effect noted here is a stark depression of void fraction, indicative of a large amount of holdup and a high slip ratio due to the viscosity of the liquid phase. Error bars represent the experimental uncertainty in determining the mass of liquid trapped.
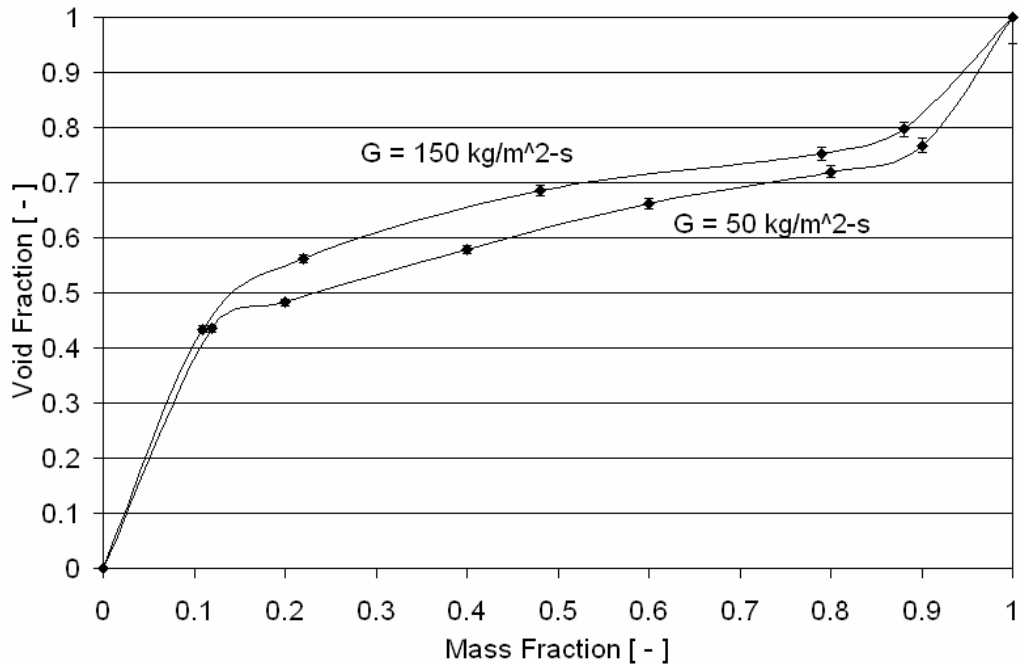
Figure 4.1: Air-ISO-32 alkylbenzene void fraction, 14-port channel.

Figure 4.2 shows in particular the effect of viscosity on void fraction, with all other parameters constant. One interesting point is that this depression seems to diminish as very high viscosities are reached, indicating a physical limit on slip and oil holdup.
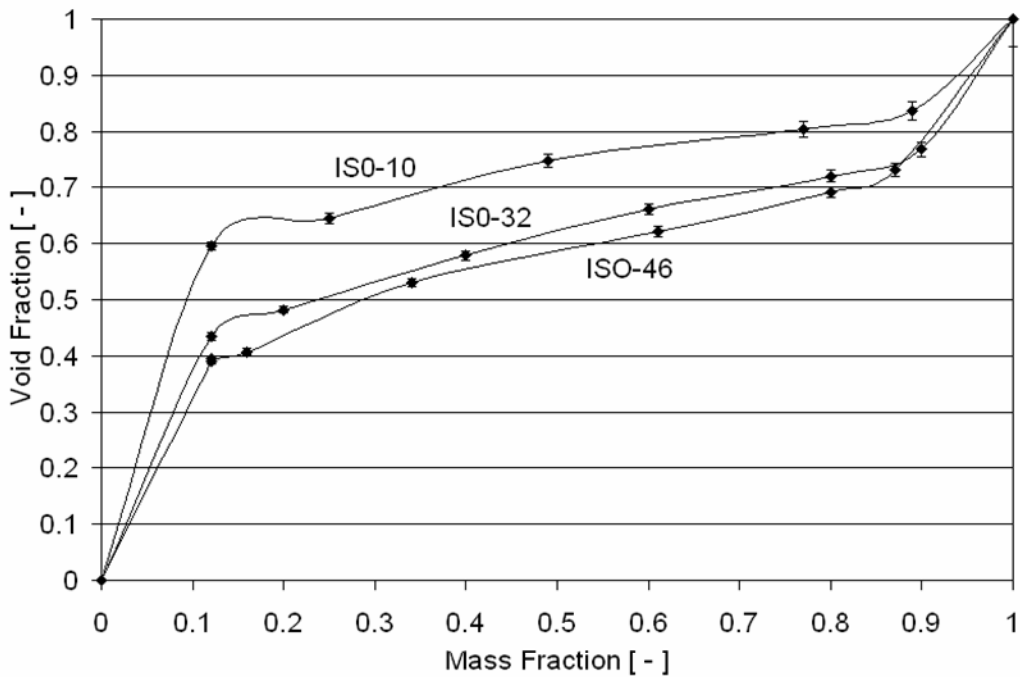
Figure 4.2: Air-alkylbenzene void fraction, G=50, 14-port channel.

4.3 Refrigerant-Oil Results

      Using the same parameters as for the pressure drop testing, a combination of R22 and ISO-32 alkylbenzene (36.3% by mass in the liquid phase) was used for void fraction experimentation over a significant number of trials, as shown in Figure 4.3. One complication in these trials was that the flow trapping mechanism was unable to trap the refrigerant sufficiently, and thus only the oil was left behind. However, because the oil/refrigerant liquid combination's concentration was measured, it was possible to deduce the void fraction from the oil holdup by accounting for the appropriate ratio of oil to refrigerant in the liquid phase. The significant divergence in void fraction values shown in Figure 4.3 points to unsteadiness in the flow distribution across the multiple ports. Figure 4.4 shows that these data are roughly bounded on the low end by the results from the highly viscous air- oil experimentation, and on the high end by the predictive correlations described above. However, the correlations over-predict the results – even the ACRC correlation which includes the relative viscosities of the two phases. Thus, further development is needed to reliably predict void fraction based on increased liquid-phase viscosity.
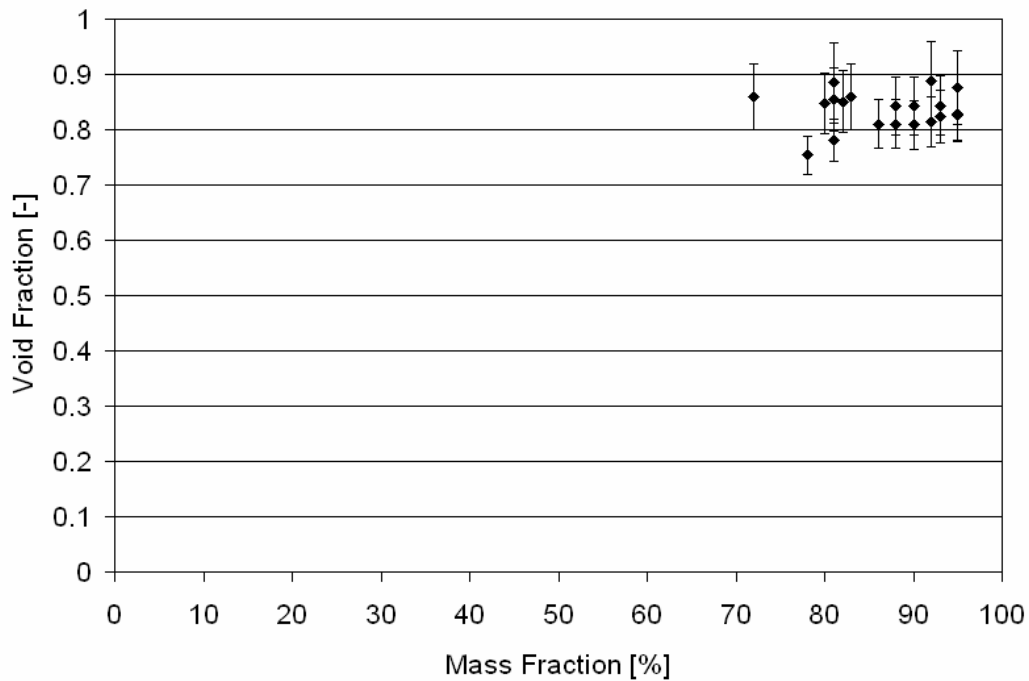
Figure 4.3: R22 void fraction with 36.3% liquid ISO-32 alkylbenzene, 14-port channel.

26
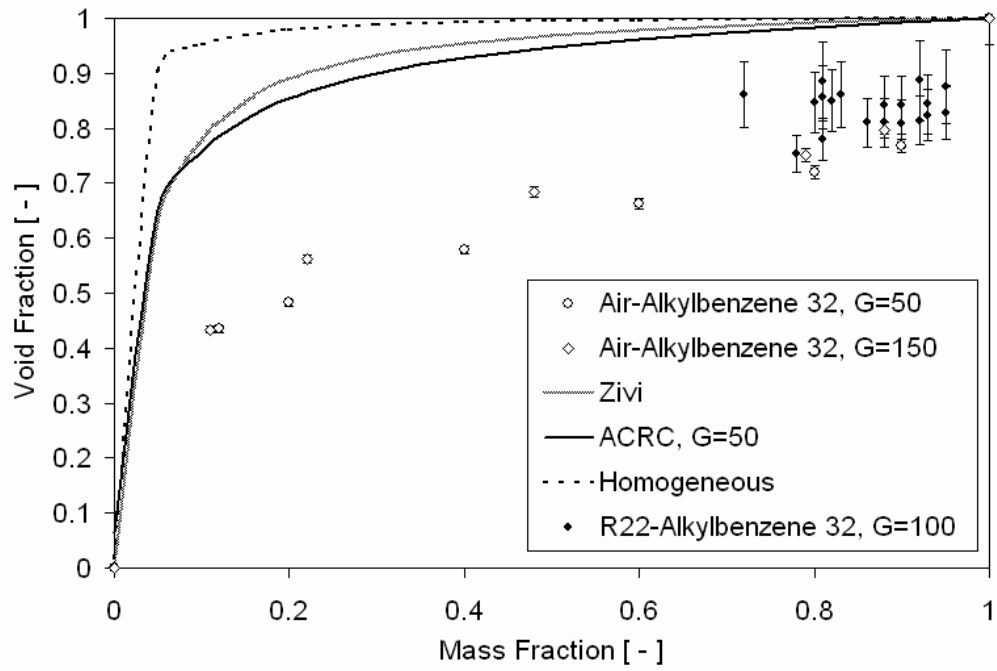
Figure 4.4: Void fraction comparison – experimental results and predictive correlations.

Chapter 5 Conclusions

5.1 Overview

Flow visualization, pressure drop, and void fraction experimentation were performed for two-phase flow in microchannels, to determine the effects of liquid-phase viscosity on the flow field. The results shed light on the impact of lubricants present in refrigeration systems, particularly the effects on system power consumption and charge requirements.

Increased viscosity was seen to restrict the flow field to primarily the separated regime, except for very low mass fractions. The presence of oil exacerbated the effects of mal-distribution among the ports of the microchannels. Greatly increased pressure drop was also noted, particularly as oil concentration and viscosity were raised. Taken together, these observations imply that the physical mechanism for this increased pressure drop occurs at the interface of the liquid and vapor phases. Void fraction is significantly depressed in the presence of a viscous liquid – indicating increased holdup within the ports, and likely leading to increased charge requirements in the case of miscible lubricant-refrigerant pairings, and an increased incidence of extreme variations in flow between ports or between channels in the system as a whole, as ports become plugged with oil.

5.2 Future Investigation

Several steps in future research will help to improve the characterization of viscous two-phase flow in microchannels. With regard to flow visualization, the development of in-situ observation techniques and computer-controlled statistical analysis will greatly contribute to the ability to predict flow regime. Improved correlations for pressure drop and void fraction should be sought out to take into account the effects demonstrated in this experiment – though the cases explored here are in some ways extreme compared to the typical viscosities encountered in a refrigeration system, the patterns indicate behavior that takes place on a smaller scale in every system where lubricant is present. Also, the use of on-line oil concentration determination will facilitate this type of experimentation on a conventional circulatory loop – increasing the ease of data collection and also the applicability of the data to real-world systems. Additionally, the nature of this study has excluded the effects of viscous two-phase flow on heat transfer, whereas future studies should naturally also include boiling and condensation as part of the heat exchanger model.

Bibliography

[1] Adams, D.C., P.S. Hrnjak and T.A. Newell. Pressure Drop and Void Fraction in Microchannels Using Carbon Dioxide, Ammonia, and R245fa as Refrigerants. ACRC TR-221. University of Illinois at Urbana-Champaign. 2003.

[2] ASHRAE Handbook. 1998 Refrigeration. ASHRAE, Atlanta, GA. 1998.

[3] Coleman, J.W. and Garimella, S. Characterization of Two-phase Flow Patterns in Small Diameter Round and Rectangular Tubes. *International Journal of Heat and Mass Transfer*, Vol. 42. 1999.

[4] Crompton, J.A., T.A. Newell, and J.C. Chato. Experimental Measurement and Modeling of Oil Holdup. ACRC TR-226. University of Illinois at Urbana-Champaign. 2004.

[5] Nino, V.G., P.S. Hrnjak and T.A. Newell. Characterization of Two-Phase Flow in Microchannels. ACRC TR-202. University of Illinois at Urbana-Champaign. 2002.

Appendix A

A.1 Air-ISO-10 Alkylbenzene Pressure Drop Data, 7.62 cm 14-Port Channel

G	X	dP	mliq	mvap
kg/m*m*s	%/100	kPa (dif)	kg/min	kg/min
51.01567	0	2.543854	0.045792	0
53	0.104198	2.86758	0.04225	0.000194
50.03544	0.211208	3.211033	0.035424	0.009487
51.06059	0.300627	4.521299	0.032053	0.01378
49.71631	0.410872	5.328986	0.026289	0.018336
50.08848	0.513466	5.375344	0.021874	0.023086
51.0752	0.586745	6.668459	0.018945	0.0269
50.32078	0.684952	7.215345	0.014231	0.030937
50.15725	0.705646	6.664191	0.013253	0.031768
49.33291	0.815062	6.167456	0.00819	0.036092
50.98716	0.883962	6.202456	0.005311	0.040455
100.3451	0	5.638483	0.09007	0
101.7902	0.104439	7.028351	0.081824	0.009543
99.76105	0.212399	12.06933	0.070525	0.01902
102.4523	0.279074	15.66046	0.066297	0.025664
100.1321	0.366616	16.21027	0.056928	0.032951
97.81351	0.405298	16.30147	0.052213	0.035584
100.2257	0.499212	19.77376	0.045052	0.04491
98.96027	0.589983	19.3561	0.036418	0.052409
100.2381	0.64441	21.29722	0.031994	0.05798
98.43707	0.733927	19.50979	0.023507	0.06485
100.0194	0.812291	20.45214	0.016854	0.072924
98.95024	0.90936	16.9413	0.008051	0.080717
150.2844	0	8.714662	0.134895	0
151.2597	0.08562	15.34114	0.124145	0.011626
148.2082	0.201141	27.88968	0.106273	0.026759
148.3311	0.309318	30.46133	0.091977	0.041165
150.3712	0.395093	34.6539	0.081655	0.053319
149.3167	0.507108	36.04922	0.06606	0.067966
149.4855	0.606739	38.435	0.052767	0.081411
150.4516	0.718228	38.51221	0.03805	0.096995
150.4922	0.8081	36.9995	0.025925	0.109157
149.828	0.887957	33.51797	0.015069	0.119417
196.8823	0	11.14237	0.176722	0
200.0765	0.110999	30.28356	0.159653	0.019936
201.1688	0.203111	37.21466	0.143893	0.036677
198.2116	0.303776	41.6644	0.12387	0.054045
200.0856	0.412647	48.28946	0.105488	0.074109
198.6732	0.504642	52.31504	0.088338	0.089991
199.7611	0.60644	53.64568	0.070568	0.108738
198.3653	0.698024	52.97955	0.053768	0.124285
200.4317	0.788233	51.09936	0.03809	0.141818
199.9898	0.896318	44.65016	0.018616	0.160895

A.2 Air-ISO-10 Alkylbenzene Pressure Drop Data, 106.68 cm 14-Port Channel

G	X	dP	mliq	mvap
kg/m*m*s	%/100	kPa (dif)	kg/min	kg/min
50.91093	0	35.63792	0.045698	0
49.59217	0.150455	53.83231	0.037964	0.0067
50.50912	0.225726	66.37065	0.035103	0.010234
50.7858	0.288021	71.04461	0.032454	0.013131
48.83853	0.308542	64.88668	0.030312	0.013526
50.20537	0.406448	77.66111	0.026747	0.018318
50.36993	0.523799	85.24088	0.02153	0.023682
51.69346	0.622154	91.37624	0.017531	0.028868
50.22132	0.71929	86.85263	0.012654	0.032424
49.9672	0.774085	85.69404	0.010133	0.034718
50.29204	0.858513	77.39346	0.006385	0.038154
99.9368	0	68.22434	0.089703	0
101.4649	0.084564	103.272	0.083716	0.007702
99.6202	0.197566	139.5547	0.071752	0.017667
100.0436	0.303446	165.0773	0.06255	0.027249
99.06424	0.412094	181.9432	0.052277	0.036644
100.2548	0.528402	199.8135	0.042437	0.047552
98.67579	0.631187	199.7908	0.032667	0.055905
101.1847	0.72616	203.4082	0.024872	0.065951
100.4044	0.795928	196.8146	0.018391	0.071732
99.86198	0.893546	170.9931	0.009542	0.080094
150.5305	0	96.87549	0.135116	0
150.262	0.101009	174.7035	0.12125	0.013625
149.4416	0.201049	217.4044	0.10717	0.026969
149.318	0.294599	244.2279	0.094545	0.039482
146.2282	0.302708	243.9711	0.091524	0.039731
151.2491	0.379291	270.068	0.084268	0.051494
148.9378	0.493058	287.4636	0.067773	0.065913
149.457	0.608454	309.0616	0.052529	0.081624
149.9303	0.690339	320.578	0.04167	0.092907
149.6476	0.842398	304.5888	0.021168	0.113156
148.0829	0.893169	281.3319	0.0142	0.118719
198.0954	0	127.0919	0.177811	0
198.6551	0.102059	240.1575	0.160115	0.018198
198.8335	0.216788	288.3313	0.139783	0.03869
200.6894	0.299664	303.6612	0.126158	0.05398
198.4159	0.403214	328.5377	0.106287	0.071811
200.1082	0.499834	356.2709	0.089839	0.089779
201.8024	0.592959	390.6748	0.073731	0.107407
197.3255	0.699575	414.618	0.053211	0.123908
198.2863	0.795252	422.8334	0.036442	0.14154
201.9939	0.913101	379.0664	0.015755	0.165554

A.3 Air-ISO-32 Alkylbenzene Pressure Drop Data, 7.62 cm 14-Port Channel

G	X	dP	mliq	mvap
kg/m*m*s	%/100	kPa (dif)	kg/min	kg/min
49.28336	0	8.31287	0.044237	0
51.21842	0	8.525645	0.045974	0
46.50201	0.087527	12.71653	0.04174	0.004
50	0.085	11.1911	0.040934	0.000165
50.35892	0.171437	13.42167	0.037436	0.007749
50.83751	0.205252	10.44083	0.036277	0.009366
50.46111	0.285586	14.95016	0.032359	0.012935
49.84464	0.304701	16.33489	0.031108	0.013633
50.35456	0.401576	13.50232	0.027048	0.01815
50.35476	0.418714	15.54362	0.026273	0.018925
50.58373	0.502441	17.85541	0.022591	0.022813
50.27458	0.593186	17.91438	0.018358	0.026768
49.90432	0.724484	16.44447	0.012342	0.032452
50.06874	0.80243	13.98451	0.008879	0.036063
50	0.889178	11.88293	0.004988	0.039913
50.01455	1	4.776794	0	0.044893
50.79535	1	4.635843	0	0.045594
51.05465	1	3.886985	0	0.045827
99.20907	0	16.86852	0.08905	0
100.3386	0.087875	22.13873	0.08216	0.007914
101.0655	0.203433	30.44092	0.072262	0.018455
100.9271	0.300535	35.29947	0.063366	0.027226
101.0497	0.404076	38.41752	0.054052	0.036651
100.8294	0.490984	41.05291	0.046068	0.044436
100.7395	0.596999	40.69754	0.036441	0.053983
101.2357	0.691778	39.81335	0.028008	0.062861
100.4778	0.802504	37.36361	0.017812	0.072377
99.9425	0.885138	31.92849	0.010304	0.079404
100.8696	0.94	27.02987	0.005432	0.085114
97.65418	1	23.79514	0.001722	0.125741
100.3872	1	10.30986	0	0.090107
100.3947	1	7.869309	0	0.090114
148.9742	0	22.06829	0.133719	0
149.6403	0.068253	33.75386	0.125094	0.009167
150.9514	0.120299	40.20075	0.119194	0.0163
149.3133	0.216769	48.64424	0.104972	0.029051
150.0158	0.319854	54.32029	0.091585	0.043069
149.4089	0.408599	59.71771	0.079313	0.054797
149.4078	0.506048	62.16603	0.066243	0.067865
149.8848	0.607166	64.07184	0.052851	0.081686
149.9606	0.716327	61.35356	0.038185	0.09642
149.7499	0.804825	56.27125	0.026235	0.10818
148.4359	0.892942	46.85314	0.014264	0.118972
150.6933	0.933109	40.85074	0.009048	0.126212
149.878	1	12.43613	0	0.134531

A.4 Air-ISO-32 Alkylbenzene Pressure Drop Data, 106.68 cm 14-Port Channel

G	X	dP	mliq	mvap
kg/m*m*s	%/100	kPa (dif)	kg/min	kg/min
49.99473	0	109.9788	0.044875	0
50.64698	0.114773	122.391	0.040282	0.005217
51.80874	0.176118	137.8689	0.038314	0.00819
48.59504	0.249494	137.4308	0.032737	0.010882
50.45864	0.339535	144.3272	0.029915	0.015377
50.07621	0.458093	161.7794	0.024358	0.02059
50.81603	0.538444	167.0054	0.021053	0.024559
50.16878	0.644022	166.9392	0.016031	0.029001
50.80657	0.760043	164.2087	0.010943	0.034661
50.46923	0.834056	148.5139	0.007518	0.037765
49.73813	1	32.25782	0	0.044645
100.1873	0	226.4292	0.089928	0
100.548	0.098791	248.9365	0.08138	0.008917
99.82663	0.188849	269.1931	0.072683	0.016921
101.4992	0.29454	301.6958	0.064272	0.026834
101.6789	0.399585	334.1765	0.054799	0.036468
100.9388	0.477154	354.9743	0.047371	0.043231
98.74285	0.592138	370.3189	0.03615	0.052482
99.07033	0.72502	368.2347	0.024453	0.064473
97.4701	0.803843	342.8557	0.017162	0.070328
104.9991	0.885349	322.8775	0.010805	0.083443
99.97572	1	68.08811	0	0.089738
148.8727	0	334.2329	0.133628	0
154.5548	0.064916	354.1164	0.130294	0.009001
152.5355	0.093982	359.7295	0.12405	0.012866
150.3665	0.142177	380.7235	0.115781	0.019188
151.5777	0.2538	416.9057	0.101526	0.03453
148.9876	0.370214	456.2324	0.084225	0.049506
151.1543	0.475022	498.2737	0.071229	0.064447
151.1483	0.582302	533.8156	0.05667	0.079001
147.1118	0.701727	538.6853	0.039386	0.092661
148.2651	0.803465	527.6221	0.026156	0.106927
149.8864	0.926906	413.8035	0.009834	0.124704
150.3419	1	105.5676	0	0.134947

A.5 Air-ISO-46 Alkylbenzene Pressure Drop Data, 7.62 cm 14-Port Channel

G	X	dP	mliq	mvap
kg/m*m*s	%/100	kPa (dif)	kg/min	kg/min
51.48889	0	13.67285	0.046216	0
50.09335	0.1169	16.54393	0.038499	0.005257
49.97862	0.213144	17.56475	0.035296	0.009564
49.2007	0.295136	19.86383	0.031128	0.013035
50.77199	0.391688	19.99042	0.027717	0.017856
49.82993	0.467961	20.91504	0.023795	0.020932
49.81857	0.588485	20.50376	0.018401	0.026316
49.41401	0.717569	19.61309	0.012527	0.031827
51.30138	0.817471	20.15791	0.008406	0.037681
48.62989	0.85696	15.79498	0.006245	0.037354
99.67805	0	28.05448	0.089471	0
100.5565	0.136546	42.02357	0.077933	0.012327
98.75816	0.215186	40.45817	0.06957	0.019075
99.68994	0.325366	44.48872	0.060366	0.029116
99.57673	0.42349	50.67888	0.051528	0.037852
99.41636	0.515788	49.57159	0.043208	0.046028
99.76629	0.609425	53.24715	0.034973	0.054577
99.12249	0.694789	47.83666	0.027155	0.061818
100.4575	0.780217	47.68041	0.019818	0.070353
99.9599	0.873818	38.95576	0.011322	0.078402

A.6 Air-ISO-46 Alkylbenzene Pressure Drop Data, 106.68 cm 14-Port Channel

G	X	dP	mliq	mvap
kg/m*m*s	%/100	kPa (dif)	kg/min	kg/min
49.75437	0	179.0055	0.04466	0
50	0.1	183.2617	0.038696	0
50.09106	0.190369	202.747	0.036402	0.008559
50.87213	0.205165	201.6759	0.036206	0.009365
49.94742	0.28342	209.8455	0.032126	0.012707
47.39519	0.312589	199.5788	0.029245	0.013297
49.32037	0.403435	218.9346	0.02641	0.017859
49.70683	0.482582	230.6625	0.023087	0.02153
51.17335	0.587809	242.0716	0.018934	0.027
49.99937	0.699914	228.9633	0.013467	0.031412
49.92455	0.808123	204.9431	0.008598	0.036214
50	0.9	167.7497	0	0.039812
99.43616	0	370.3884	0.089254	0
97.65965	0.096604	358.3038	0.079316	0.008465
97.91006	0.177563	377.4864	0.072281	0.015603
97.35552	0.329264	439.5055	0.058616	0.02877
100.1525	0.385775	473.2178	0.055217	0.03468
99.81377	0.495946	502.8455	0.045158	0.044435
99.90944	0.597531	514.1944	0.036094	0.053585
102.6216	0.691225	518.541	0.028443	0.06367
100.8777	0.808973	464.1406	0.017296	0.073252
97.68703	0.90306	356.6058	0.008499	0.079185

A.7 Air-ISO-68 Alkylbenzene Pressure Drop Data, 7.62 cm 14-Port Channel

G	X	dP	mliq	mvap
kg/m*m*s	%/100	kPa (dif)	kg/min	kg/min
50.49369	0	20.92024	0.045323	0
49.7188	0.124863	29.22978	0.039046	0.005572
50.88686	0.183904	30.82178	0.03732	0.0084
50.19301	0.30135	29.01889	0.031477	0.013577
50.28374	0.391421	32.38023	0.027468	0.017666
49.94492	0.470435	32.14109	0.023741	0.02109
50.64432	0.605868	31.60304	0.017916	0.027542
50.14525	0.716838	28.28009	0.012745	0.032265
50.1115	0.778095	27.05912	0.009981	0.034999
50.73085	0.861075	23.63588	0.006326	0.039213
51.14713	0.932475	19.68209	0.0031	0.042809
50.69994	1	4.251902	0	0.045508

A.8 Air-ISO-68 Alkylbenzene Pressure Drop Data, 106.68 cm 14-Port Channel

G	X	dP	mliq	mvap
kg/m*m*s	%/100	kPa (dif)	kg/min	kg/min
50.11533	0	329.4226	0.044983	0
48.84597	0.121858	312.2888	0.03757	0.005297
50.48883	0.225222	331.2674	0.035118	0.010201
49.41266	0.323567	329.7457	0.030008	0.014346
50.04147	0.420335	342.7172	0.026041	0.018876
48.96313	0.498803	336.7383	0.022032	0.021917
48.93269	0.621131	324.4874	0.016643	0.027279
49.30674	0.696617	312.8742	0.013429	0.030829
50.25543	0.807615	276.6905	0.008678	0.036429
50.45923	0.902851	225.2212	0.0044	0.040891
50.07716	1	35.71137	0	0.044949
49.31441	0	325.9387	0.044265	0
52.36349	0.18823	340.6339	0.038149	0.008841
51.25552	0.263414	338.2114	0.033898	0.012109
52.75747	0.521683	365.4415	0.022659	0.024696
50.54512	0.76553	300.1036	0.010639	0.034731
51.00157	0.899517	225.6149	0.0046	0.041179

A.9 R22 Pressure Drop Data, 7.62 cm 14-Port Channel

G	X	dP	mliq	mvap	hliq	hvap	hmix
kg/m*m*s	%/100	kPa (dif)	kg/min	kg/min	kJ/kg	kJ/kg	kJ/kg
49.99097	0	0.085957	0.050061	0	225.2525	415.4344	225.2525
50.27602	0.747788	0.371761	0.014251	0.036095	225.945	413.3983	360.345
51.07674	0	0.16989	0.051148	0	226.1493	413.2256	226.1493
49.20671	1	0.284855	0	0.049276	226.3823	412.9196	412.9196
49.46667	1	0.400425	0	0.049536	226.1546	413.5941	413.5941
49.04149	0.248735	0.209188	0.039374	0.009736	226.2909	412.8536	263.2772
53.97337	0.416854	0.280317	0.033454	0.020595	226.2145	413.5604	297.5978
49.96691	0.850137	0.343421	0.009001	0.041043	226.2617	414.4858	382.4284
97.06813	1	0.767851	0	0.097204	225.9459	415.4041	415.4041
100.7735	0.279116	0.538614	0.078261	0.022654	225.6245	413.5454	267.8286
102.2917	0.50604	0.712499	0.055036	0.047398	225.8493	414.6809	313.2249
99.28326	0.823022	0.675754	0.019661	0.079761	225.9313	413.3218	376.263
99.00191	0	0.265322	0.09914	0	226.3917	414.234	226.3917
149.4829	0	0.516742	0.149692	0	224.6234	416.5323	224.6234
150.5238	0	0.381748	0.150735	0	226.6895	426.6837	226.6895
151.5046	0	0.563111	0.151717	0	225.3106	414.7078	225.3106
157.0499	0	0.734785	0.15727	0	224.7145	414.7642	224.7145
149.2458	0.312131	0.936952	0.107776	0.041679	225.2332	413.3341	277.6978
149.7141	0.489511	1.01624	0.080958	0.068966	225.4426	413.7333	312.0508
150.3104	0.703286	1.090724	0.048155	0.102366	225.6406	413.9859	353.6896

A.10 R22 Pressure Drop Data, 106.68 cm 14-Port Channel

G	X	dP	mliq	mvap	hliq	hvap	hmix
kg/m*m*s	%/100	kPa (dif)	kg/min	kg/min	kJ/kg	kJ/kg	kJ/kg
50.19037	0	1.305051	0.050261	0	224.5	417.9808	224.5
49.75552	1.000166	2.759674	0	0.049825	225.6541	411.3452	411.3452
51.46809	0	0.508785	0.05154	0	211.3484	412.1726	211.3484
51.23523	0.170815	1.644	0.045888	0.005419	226.1738	414.3288	245.6307
52.8952	0.18614	1.2895	0.045894	0.007075	226.852	413.122	251.7347
49.35034	0.458761	1.197648	0.027031	0.022389	226.6439	413.2712	311.2023
48.83528	0.589113	1.948	0.021608	0.027296	226.9707	413.0211	330.8173
49.30501	0.676663	1.894	0.017489	0.031885	226.9834	412.9418	347.0709
49.66541	0.829248	2.082	0.009742	0.039993	227.1729	413.4975	377.0167
48.39754	0.53082	1.846243	0.024207	0.024258	225.7205	412.6268	319.3033
51.22727	0.373275	1.412959	0.034691	0.016608	225.9641	412.2914	286.2944
49.31757	0.656222	1.876319	0.01841	0.030976	225.9938	412.2289	342.8114
49.06193	0.805955	1.596577	0.010839	0.038292	226.0102	412.3068	371.4025
49.61498	0.352619	1.353203	0.03444	0.015244	225.579	412.4416	282.9339
50.74456	0.263909	1.018775	0.040545	0.01027	225.7	412.581	263.4803
49.46653	0	0.866775	0.049536	0	225.2086	412.2581	225.2086
99.35929	0.71258	7.245892	0.031246	0.068252	226.3031	414.6347	355.4988
98.29285	0.896665	8.368035	0.013764	0.084667	226.1247	414.7428	388.3588
100.2414	0	2.035812	0.100382	0	224.4332	418.0445	224.4332
99.39593	1	8.552566	0	0.099535	225.8075	415.2345	415.2345
98.49853	0.443501	6.180807	0.057988	0.040648	224.5564	413.4234	302.3887
99.87853	0.330287	4.108163	0.073689	0.026329	225.2485	414.0033	274.935
100.9694	0.20689	4.011823	0.089095	0.012016	225.2924	413.1827	247.6299
100.0577	0.601376	5.993927	0.044909	0.055289	226.1342	414.7761	330.2189
103.0031	0.187637	3.304428	0.078899	0.013557	226.5409	413.1816	253.8886
99.94576	0.284775	4.20245	0.075419	0.024667	226.7898	412.9991	272.6536
102.7	0.415001	6.078071	0.065235	0.037609	226.8572	414.9124	295.6182
98.69126	0.430221	5.132	0.061489	0.037341	226.0215	414.07	297.0712
100.4176	0.183051	3.110983	0.088785	0.01292	226.2914	412.3189	244.3194
95.99453	0.606824	6.034481	0.035023	0.051142	225.7597	412.1513	336.3781
149.8679	0	2.896536	0.150078	0	226.1977	411.4825	226.1977
147.491	0.154097	6.22906	0.138809	0.008916	225.3721	412.3669	235.8542
151.5943	0.20163	6.737425	0.130724	0.021082	226.4516	411.4039	252.1371
150.4493	0.333657	8.986787	0.109726	0.040934	227.1318	411.4536	277.2081
149.4072	0.522735	10.2609	0.078542	0.071074	226.5933	413.8338	315.5241
149.9249	0.925656	15.55332	0.018729	0.131406	225.4772	417.2236	393.2896
149.9197	0.084394	2.669417	0.15013	0	223.9053	418.351	223.9053
149.6747	1	16.11653	0	0.149884	225.8598	416.03	416.03
150.8877	0.165135	4.93571	0.133387	0.017712	226.4109	412.2577	248.1967
148.4128	0.285782	6.526175	0.111663	0.036958	226.2047	412.0138	272.4174
149.0423	0.503668	10.57912	0.079656	0.069595	225.8541	412.9888	313.1008
147.5573	0.723275	12.21878	0.045395	0.10237	226.0356	413.2087	355.7041

A.11 R22-ISO-10 Alkylbenzene Pressure Drop Data, 7.62 cm 14-Port Channel

G	X	dP	mliq	mvap
kg/m*m*s	%/100	kPa (dif)	kg/min	kg/min
98.03435	0.723298	1.157958	0.027174	0.070998
99.84696	0.761221	1.679416	0.023879	0.076108
96.48018	0.84425	1.695428	0.015053	0.081563
99.44695	0.869833	1.929952	0.012965	0.086621
99.36009	0.898284	1.58517	0.010125	0.089374
96.94627	0.931517	0.938002	0.006653	0.090609

A.12 R22-ISO-10 Alkylbenzene Pressure Drop Data, 106.68 cm 14-Port Channel

G	X	dP	mliq	mvap
kg/m*m*s	%/100	kPa (dif)	kg/min	kg/min
99.18983	0.718831	24.1053	0.027934	0.071395
100.2029	0.760324	25.33113	0.024065	0.076278
100.4905	0.812345	24.44195	0.018894	0.081737
98.28881	0.861876	22.11986	0.013598	0.084829
99.11813	0.922141	17.56909	0.007729	0.091585
99.84771	0.940717	16.38126	0.005928	0.093922
99.16981	0.947676	14.22003	0.005197	0.09389

A.13 R22-ISO-32 Alkylbenzene Pressure Drop Data, 7.62 cm 14-Port Channel

G	X	dP	mliq	mvap
kg/m*m*s	%/100	kPa (dif)	kg/min	kg/min
48.89911	0.715662	1.326378	0.013931	0.035036
48.62033	0.729941	1.003272	0.013154	0.035534
50.70563	0.788772	0.87278	0.010728	0.040049
50.0663	0.830592	0.99775	0.008543	0.041826
49.58465	0.890876	0.733722	0.004954	0.044196
49.83379	0.937878	0.587313	0.0031	0.046804
98.06991	0.718497	3.486065	0.027654	0.070554
98.52363	0.781818	2.275454	0.021531	0.07713
101.1407	0.813564	2.781357	0.018885	0.082398
98.11452	0.86382	2.589062	0.013384	0.084868
99.2999	0.895543	1.78159	0.010388	0.089051
100.6519	0.937288	1.574351	0.006322	0.094152
148.416	0.709787	5.674713	0.043132	0.105492
148.9191	0.767072	5.606255	0.034745	0.114383
146.2887	0.838573	4.884918	0.023656	0.122838
149.1048	0.895874	4.024669	0.015562	0.133752
148.8118	0.910056	4.548255	0.013405	0.135615
147.0407	0.940403	3.272562	0.008784	0.138463

A.14 R22-ISO-32 Alkylbenzene Pressure Drop Data, 106.68 cm 14-Port Channel

G	X	dP	mliq	mvap
kg/m*m*s	%/100	kPa (dif)	kg/min	kg/min
50.31903	0.701888	12.44946	0.015022	0.035368
51.58833	0.777905	10.20525	0.011475	0.040185
49.04095	0.877726	6.872325	0.00601	0.043012
50.65646	0.938889	7.21192	0.0031	0.047627
48.55803	0.858706	9.651142	0.006871	0.041747
100.375	0.736337	33.23941	0.026508	0.074008
96.99286	0.850905	27.3449	0.014482	0.082646
96.00805	0.943547	17.4097	0.005428	0.090916
99.53538	0.876404	26.98195	0.012321	0.087354
98.07317	0.814506	30.09684	0.01822	0.07999
148.7264	0.718696	63.99102	0.041909	0.107026
147.696	0.810237	55.96664	0.028071	0.119832
147.5408	0.853608	50.88046	0.021632	0.126115
149.7389	0.917037	44.23525	0.012443	0.137505
147.6887	0.96284	34.84573	0.005496	0.142813

A.15 R134A-ISO-32 Alkylbenzene Pressure Drop Data, 7.62 cm 14-Port Channel

G	X	dP	mliq	mvap
kg/m*m*s	%/100	kPa (dif)	kg/min	kg/min
49.94487	0.739857	2.581766	0.013013	0.037002
48.62851	0.881927	0.835004	0.00575	0.041048
46.66013	0.874731	2.229393	0.005867	0.040682
47.04412	0.798196	0.599659	0.009552	0.037557

A.16 R134A-ISO-32 Alkylbenzene Pressure Drop Data, 106.68 cm 14-Port Channel

G	X	dP	mliq	mvap
kg/m*m*s	%/100	kPa (dif)	kg/min	kg/min
50.3056	0.834964	29.4869	0.008321	0.042097
50.72694	0.936961	14.55694	0.0032	0.047598
49.16429	0.853896	25.73489	0.007196	0.041903
50.05404	0.893988	16.04564	0.005309	0.043434
46.6854	0.885014	20.45687	0.00485	0.04144
46.92166	0.7694	27.49335	0.010858	0.03613
48.56741	0.81467	26.76655	0.009022	0.039614

A.17 R134A-ISO-32 POE Pressure Drop Data, 7.62 cm 14-Port Channel

G	X	dP	mliq	mvap
kg/m*m*s	%/100	kPa (dif)	kg/min	kg/min
49.10878	0.767761	1.186276	0.011423	0.037755
48.16113	0.823176	1.031491	0.008529	0.039732
48.95198	0.834615	1.063019	0.008111	0.040871
48.84856	0.856149	0.302402	0.007038	0.041796
48.31076	0.886254	1.124995	0.005507	0.042878
48.75165	0.926253	1.093121	0.0036	0.04522
48.58428	1	0.676902	0	0.048652

A.18 R134A-ISO-32 POE Pressure Drop Data, 106.68 cm 14-Port Channel

G	X	dP	mliq	mvap
kg/m*m*s	%/100	kPa (dif)	kg/min	kg/min
50.70874	0.739801	22.73988	0.013219	0.037561
48.71583	0.795353	19.2317	0.009986	0.038798
50.75543	0.837259	18.49941	0.008275	0.042541
51.5736	0.839636	22.89693	0.008283	0.043363
49.91946	0.874085	15.05254	0.006296	0.043641
50.84912	0.921444	15.23384	0.004	0.04692
50.10685	1	5.563581	0	0.050177

Appendix B

B.1 Air-Alkylbenzene Void Fraction Data, 106.68 cm 14-Port Channel

		X [g]	Total Mass [g]	Void Fraction [-]	Uncertainty [-]
ISO-10	G=50	0.12	63.21	0.596	0.008
ISO-10	G=50	0.25	62.59	0.644	0.009
ISO-10	G=50	0.49	61.26	0.748	0.012
ISO-10	G=50	0.77	60.54	0.805	0.014
ISO-10	G=50	0.89	60.14	0.836	0.016
ISO-10	G=150	0.1	63.13	0.602	0.008
ISO-10	G=150	0.21	62.19	0.676	0.010
ISO-10	G=150	0.51	60.81	0.783	0.013
ISO-10	G=150	0.8	60.12	0.837	0.016
ISO-10	G=150	0.91	59.49	0.887	0.020
ISO-32	G=50	0	70.83	0.000	
ISO-32	G=50	0.12	65.27	0.435	0.006
ISO-32	G=50	0.2	64.66	0.482	0.007
ISO-32	G=50	0.4	63.43	0.579	0.008
ISO-32	G=50	0.6	62.36	0.662	0.009
ISO-32	G=50	0.8	61.62	0.720	0.011
ISO-32	G=50	0.9	61.01	0.768	0.012
ISO-32	G=50	1	58.04	1.000	
ISO-32	G=150	0.11	65.28	0.434	0.006
ISO-32	G=150	0.22	63.64	0.562	0.008
ISO-32	G=150	0.48	62.07	0.685	0.010
ISO-32	G=150	0.79	61.22	0.751	0.012
ISO-32	G=150	0.88	60.64	0.797	0.014
ISO-46	G=50	0.12	65.84	0.390	0.006
ISO-46	G=50	0.12	65.79	0.394	0.006
ISO-46	G=50	0.16	65.62	0.407	0.006
ISO-46	G=50	0.34	64.06	0.529	0.007
ISO-46	G=50	0.61	62.88	0.622	0.009
ISO-46	G=50	0.8	61.98	0.692	0.010
ISO-46	G=50	0.87	61.48	0.731	0.011

B.2 R22-Alkylbenzene Void Fraction Data, 106.68 cm 14-Port Channel

Mass (empty) [g]	Mass (total) [g]	Mass (oil trapped) [g]	Mass (liquid, est.) [kg]	Volume (liquid, est.) [m^3]	Liquid Fraction [-]	Void Fraction [-]	Uncertainty [-]
57.76	58.9	1.14	3.032E-03	3.032E-06	0.189	0.811	0.044
57.76	58.79	1.03	2.739E-03	2.739E-06	0.171	0.829	0.049
57.8	59.12	1.32	3.511E-03	3.511E-06	0.219	0.781	0.038
57.81	58.95	1.14	3.032E-03	3.032E-06	0.189	0.811	0.044
57.75	58.67	0.92	2.447E-03	2.447E-06	0.153	0.847	0.054
57.75	59.23	1.48	3.936E-03	3.936E-06	0.246	0.754	0.034
57.77	58.81	1.04	2.766E-03	2.766E-06	0.173	0.827	0.048
57.76	58.63	0.87	2.314E-03	2.314E-06	0.145	0.855	0.057
57.76	58.6	0.84	2.234E-03	2.234E-06	0.140	0.860	0.060
57.74	58.68	0.94	2.500E-03	2.500E-06	0.156	0.844	0.053
57.74	58.69	0.95	2.527E-03	2.527E-06	0.158	0.842	0.053
57.78	58.9	1.12	2.979E-03	2.979E-06	0.186	0.814	0.045
57.79	58.94	1.15	3.059E-03	3.059E-06	0.191	0.809	0.043
57.72	58.56	0.84	2.234E-03	2.234E-06	0.140	0.860	0.060
57.7	58.6	0.9	2.394E-03	2.394E-06	0.150	0.850	0.056
57.75	58.81	1.06	2.819E-03	2.819E-06	0.176	0.824	0.047
57.76	58.44	0.68	1.809E-03	1.809E-06	0.113	0.887	0.074
57.74	58.69	0.95	2.527E-03	2.527E-06	0.158	0.842	0.053
57.79	58.54	0.75	1.995E-03	1.995E-06	0.125	0.875	0.067
57.77	58.46	0.69	1.835E-03	1.835E-06	0.115	0.885	0.072